Variations in wave slope and momentum flux from wave-current interactions in the tropical trade winds

Suneil Iyer[1,2], Jim Thomson[1], Elizabeth Thompson[3], Kyla Drushka[1,2]

[1]Applied Physics Laboratory, University of Washington, Seattle, Washington, USA
[2]School of Oceanography, University of Washington, Seattle, Washington, USA
[3]NOAA Physical Sciences Laboratory, Boulder, Colorado, USA

Key Points:

- Six Lagrangian surface drifters observed wave spectra in an area of moderate mesoscale activity in the northwestern tropical Atlantic.
- Surface current and wind-wave directions were opposed over 10% of the time; during this time wave mean square slope was elevated.
- Wave-current interactions caused variations in air-sea momentum flux of up to 30%.

Corresponding author: Suneil Iyer, `iyersk@uw.edu`

Abstract

Observations from six Lagrangian Surface Wave Instrument Float with Tracking (SWIFT) drifters in January-February 2020 in the northwestern tropical Atlantic during the Atlantic Tradewind Ocean-atmosphere Mesoscale Interaction Campaign (ATOMIC) are used to evaluate the influence of wave-current interactions on wave slope and momentum flux. At wind speeds of 4-12 ms^{-1}, wave mean square slopes are positively correlated with wind speed. Wave-relative surface currents varied significantly, from opposing the wave direction at 0.16 ms^{-1} to following the waves at 0.57 ms^{-1}. For a given wind speed, wave slopes are up to 20% higher when surface currents oppose the waves compared to when currents strongly follow the waves, consistent with a theoretical Doppler shift between the absolute (fixed) and intrinsic (relative) frequency. Assuming an equilibrium frequency range in the wave spectrum, wave slope is proportional to wind friction velocity and momentum flux. The observed variation in wave slope equates to up to a 40% variation in momentum flux for a given wind speed. This is 30% greater than the variation expected from current-relative winds alone, and suggests that wave-current interactions can generate significant spatial and temporal variability in momentum fluxes in this region of prevailing trade winds. Results and data from this study motivate the continued development of fully coupled atmosphere-ocean-wave models.

Plain Language Summary

Six surface current-following drifters were deployed in the northwestern tropical Atlantic during the Atlantic Tradewind Ocean-atmosphere Mesoscale Interaction Campaign (ATOMIC) to study how surface currents influence wave properties. In theory, surface currents in the opposite direction as the waves will cause a shift in wave frequency leading to wave steepening. Increased wave slopes, due to opposing surface currents, may lead to increased whitecapping and wave breaking. Similarly, surface currents in the same direction as the waves are expected to flatten waves. Wind directions were relatively constant, owing to prevailing trade winds. Wave slopes varied by up to 20% at at a given wind speed due to the variability of surface currents. This suggests that surface currents may influence air-sea exchanges of gas, heat, and momentum through their interaction with waves. The effect of surface currents on waves is often not incorporated into model parameterizations, so these findings may be useful in the development of more fully coupled atmosphere-ocean-wave models.

1 Introduction

1.1 Importance and Background

Air-sea interactions are an important component of the global climate system, as they modulate the transfer of heat, buoyancy, momentum, and gases between the atmosphere and the ocean and are a driving force behind creating boundary layer to multidecadal-scale patterns in weather and climate. Surface gravity waves are a key component of the air-sea interface and modulate the transfer of momentum from the atmosphere to the ocean through modification of surface drag (e.g., Janssen, 1989, and others), energy injection from breaking (e.g., Craig & Banner, 1994, and others), and momentum storage in the wave field (e.g., Ardhuin et al., 2004; Fisher et al., 2017, and others). Existing work on the role of waves in air-sea interaction often parameterizes this process using a wind speed-dependent drag coefficient (Smith, 1980; Large & Pond, 1981; Edson et al., 2013), or incorporates waves only through a wave age parameterization, which has been found to produce similar results as parameterizations incorporating wind speed alone (Edson et al., 2013). While these assumptions may be reasonable when waves are modified only by wind and when wind-wave equilibrium (Phillips, 1985) holds, significant uncertainties exist when other processes affect surface waves. A primary objective of the present study is to evaluate the significance of wave-current interactions, which are not typically

incorporated into model parameterizations on wave properties and momentum flux at small scales. Another focus is to compare observations with momentum flux calculated using the COARE bulk flux algorithm (Fairall et al., 1996, 2003; Edson et al., 2013), a widely-used scheme which incorporates current and wave effects on stress through current-relative winds and wave age, respectively, but does not parameterize wave-current interactions. It is well documented that surface currents vary at the mesoscale and smaller scales due to eddies and fronts (e.g., Molinari et al., 1981; Ebuchi & Hanawa, 2000; van Aken, 2002; Kim, 2010; McWilliams, 2016, and others); presumably, these current variations would lead to spatial differences in wave-current interactions and momentum flux.

In theory, a Doppler shift will modify the wavenumber and wave speed by an amount depending on the alignment of the surface current and the waves. Because the surface energy flux of waves is conserved, this will elevate wave slopes when surface currents are in the opposite direction as the waves, and decrease wave slopes when wave and current directions are aligned. The frequency shift is caused by the projection of the current vector onto the wave direction; this component will hereinafter be referred to as the wave-relative current. In areas where currents are spatially variable such as across fronts, wave slopes would be expected to vary on those same spatial scales. This has been observed in the field (Thomson et al., 2014; Zippel & Thomson, 2017; Branch et al., 2018; Kastner et al., 2018; Gemmrich & Pawlowicz, 2020) and simulated by numerical models (Akan et al., 2017, 2018; Moghimi et al., 2019) in coastal areas where strong spatial current variability exists. Specifically, energy levels, significant wave height, whitecapping, wave breaking, and near-surface turbulent dissipation rates are elevated where currents oppose the waves due to wave steepening. Wave properties can vary on spatial scales of ones to tens of km (e.g., Thomson et al., 2014; Branch et al., 2018) or larger (e.g., Gemmrich & Pawlowicz, 2020), depending on the structure of coastal features associated with current variability, including river plumes (Thomson et al., 2014; Branch et al., 2018), fronts, and upwelling jets (Romero et al., 2017). Near river mouths, currents can even be strong enough to reduce the wave group velocity to zero and block the propagation of waves on the side of a front where currents strongly oppose the waves (Chawla & Kirby, 2002; Chen & Zou, 2018).

Only a limited amount of research on wave-current interactions has focused on the open ocean, where currents are typically more wind- and wave-following than in localized coastal areas. Romero et al. (2017) quantify current effects on wave properties associated with the Loop Current in the Gulf of Mexico. Strong fronts with surface current gradients of up to 1.5 ms^{-1} over roughly 50 km exhibited variations in wave height and slope of up to 30%, with greater variation in whitecap coverage. At O(100 km) scales, storms and western boundary currents have been shown to modulate wave properties in the presence of strong surface currents (Holthuijsen & Tolman, 1991; Wang & Sheng, 2016; Hegermiller et al., 2019). Wave-current interactions have also been shown to be significant at very small scales: Rascle et al. (2017) observed sea surface roughness anomalies across a 50 m-wide submesoscale front and attribute this to strong current gradients of 0.3 ms^{-1}. These results demonstrate that wave-current interactions associated with strong surface current variability are important in the open ocean as well as coastal areas.

Wave-current interactions have been frequently studied using models. Mesoscale features on O(10-100 km scales) cause variations in wave properties through refraction, the advection of energy, the energy exchange between waves and currents, the aforementioned Doppler frequency shift, and the effect of currents on the wind stress between the ocean and atmosphere (Ardhuin et al., 2017). Romero et al. (2020) quantify some of this variability on O(1-10 km scales) with numerical modeling, and demonstrate that wave-current interactions most significantly influence wave-breaking variables including whitecap coverage and energy dissipation, particularly when winds are weak. Wave-current interactions also have a strong influence on significant wave height at scales of tens of

kilometers (Ardhuin et al., 2017; Kudryavtsev et al., 2017; Quilfen et al., 2018). Similar effects on significant wave height have been shown at the mesoscale and at larger scales: Quilfen and Chapron (2019) show that current variability on scales of hundreds of kilometers can influence wave heights, and Rapizo et al. (2018) show wave flattening on even larger scales due to wave-following currents. Non-negligible effects of currents have been observed on other bulk wave variables including wave mean square slope mss (Rascle et al., 2014; Romero et al., 2020). Current effects on waves should theoretically be more significant for wind waves having frequencies above the spectral peak (Phillips, 1984; McWilliams, 2018). While not the focus of the present study, it has been demonstrated that the reverse feedback can occur as well; i.e., waves can cause variations in surface currents (Tang et al., 2007; Suzuki et al., 2016; McWilliams, 2018). However, model results have shown that this effect is only a small contributor to submesoscale and mesoscale variability (Romero et al., 2021). Hereinafter in this manuscript, "wave-current interactions" will refer to current effects on waves, rather than wave effects on currents. A main objective of the present study is to analyze the influence of wave-current interactions on short temporal scales and spatial scales of tens of kilometers with observations. This is of similar scale to several previous modeling studies (e.g., Ardhuin et al., 2017; Romero et al., 2020), but smaller than the focus of large-scale observational studies (e.g., Holthuijsen & Tolman, 1991).

In areas with significant mesoscale or submesoscale activity, spatial gradients in currents are often associated with sea surface temperature (SST) fronts. SST fronts can generate spatial variations in air-sea heat fluxes, which can in turn modify momentum fluxes, wind, and waves. For instance, heating over the warm side of a front destabilizes the atmospheric boundary layer, which induces atmospheric convection and increases surface wind speeds through either downward momentum transfer (Wallace et al., 1989) or horizontal pressure gradients (Lindzen & Nigam, 1987). These increases in wind speed can then influence the high frequency part of the wave spectrum. The modification of air-sea fluxes by SST fronts has been observed and modeled at the submesoscale (Shao et al., 2019; Redelsperger et al., 2019) and at the mesoscale (Businger & Shaw, 1984; Friehe et al., 1991; Chelton et al., 2001, 2004; Gaube et al., 2015). The primary focus of this work will be direct effects of the currents on waves and momentum flux, but it is important to note that indirect effects such as those induced by SST fronts may also be significant.

1.2 Theory

We expect mss to vary as a result of currents opposing or following the waves, which will further influence surface stress (i.e., momentum flux). We know that

$$\tau = \rho_a u_*^2, \tag{1}$$

where

$$u_* = C_D^{1/2}(U_{10} - U cos\theta). \tag{2}$$

Parameter τ is the surface wind stress, ρ_a is the air density, u_* is the friction velocity, C_D is the drag coefficient, U_{10} is the 10 meter wind speed, U is the surface current, and θ is the angle between the surface current direction and the average wave direction in an equilibrium frequency range ($f_{max} - f_{min}$). Assuming that the source of wave energy (i.e., wind) is balanced by wave breaking and nonlinear effects (Phillips, 1984, 1985), and that the wind energy input is proportional to u_* and mss (Plant, 1982), u_* can be defined as a function of the wave energy spectrum $E(f)$, which scales with f^{-4} (Phillips, 1985; Juszko et al., 1995; Thomson et al., 2013; Voermans et al., 2020). Within the equilibrium frequency range,

$$u_* = \int_{f_{min}}^{f_{max}} \frac{E(f) f^4 2\pi^3}{\beta I(p) g (f_{max} - f_{min})} df. \tag{3}$$

Parameter f is the wave frequency, β is an empirically determined constant taken as 0.012, g is gravitational acceleration, and I is the wave directional spreading function with parameter p as defined by Phillips (1985). Following Phillips (1985), we assume a constant p=0.5 and $I(p)$=2.5. By combining the above equation with the similar relation of Kitaigorodskii (1983),

$$mss = \int_{f_{min}}^{f_{max}} \frac{E(f) f^4 16\pi^4}{g^2} df, \tag{4}$$

u_* can be related to mss as

$$\frac{u_*}{mss} = \frac{g}{8\pi\beta I(p)(f_{max} - f_{min})}. \tag{5}$$

Equation 5 demonstrates that mss and u_* are directly proportional under the assumptions that the equilibrium frequency range $f_{max}-f_{min}$, β, and $I(p)$ are constant. The present study makes these assumptions, so observations presented in terms of mss and u_* are essentially equivalent and differ only by a constant factor.

When waves encounter a uniform current in the same or opposite direction as the waves, the Doppler shift effect leads to a shift in wave frequency by an amount proportional to wavenumber and the component of the current velocity aligned with the waves (Phillips, 1984). This frequency shift can be defined using

$$\omega = \sigma + \vec{u} \cdot \vec{k} = \sigma + Ukcos(\theta), \tag{6}$$

where ω is the absolute frequency of the wave in a fixed reference frame and σ is the intrinsic frequency defined with the deep-water wave dispersion relation,

$$\sigma = 2\pi f = \sqrt{gk}. \tag{7}$$

Parameter $\vec{u}$ is the current and $\vec{k}$ is the wavenumber. Currents opposing the direction of wave propagation will cause an increase in wavenumber and decrease in wave speed proportional to the current speed. To conserve the surface energy flux of the waves, they must steepen. If waves reach a critical steepness, they can break (Phillips, 1984; van der Westhuysen, 2012; Thomson et al., 2014; Romero et al., 2017; Zippel & Thomson, 2017; Gemmrich & Pawlowicz, 2020). Similarly, currents in the same direction as the waves will experience a decrease in wavenumber, increase in wave speed, and flattening. Wave properties are further modified when strong vertical (Choi, 2009; Banihashemi et al., 2017; Ellingsen & Li, 2017; Banihashemi & Kirby, 2019) or horizontal (Haus, 2007) current shear exists. By substituting the absolute frequency (equation 6) into equation 4 and rewriting terms using equation 7, we can obtain an equation for mss (or equilibrium u_*, using equation 3),

$$mss = \int_{f_{min}}^{f_{max}} \frac{16\pi^4 f^4 E(f)}{g^2} \left(1 + \frac{8\pi f U}{g} + \frac{24\pi^2 f^2 U^2}{g^2} + \frac{32\pi^3 f^3 U^3}{g^3} + \frac{16\pi^4 f^4 U^4}{g^4}\right) df, \tag{8}$$

as a function of U and $E(f)$, which is expected to increase at increasing wind speeds (equations 2,3). Using equation 8, we can calculate an expected variation in mss or u_* when a nonzero uniform current U is imposed.

The theory suggests that the relative surface current would also contribute to variability in u_*, both by modifying the current-relative wind speed ($U_{10}-Ucos\theta$ in equation 2; Figure 1a) and through the Doppler shift effect (Figure 1b). A recent study estimated wind speed from in situ observations of wave spectra and found that observed wind speeds between 3 and 12 ms^{-1} are generally consistent with values predicted from equation 3, with uncertainty resulting from sea state and buoy motion (Voermans et al., 2020). While wave properties vary significantly due to the Doppler shift effect in coastal regions where surface currents are strong and variable (Thomson et al., 2014; Campana

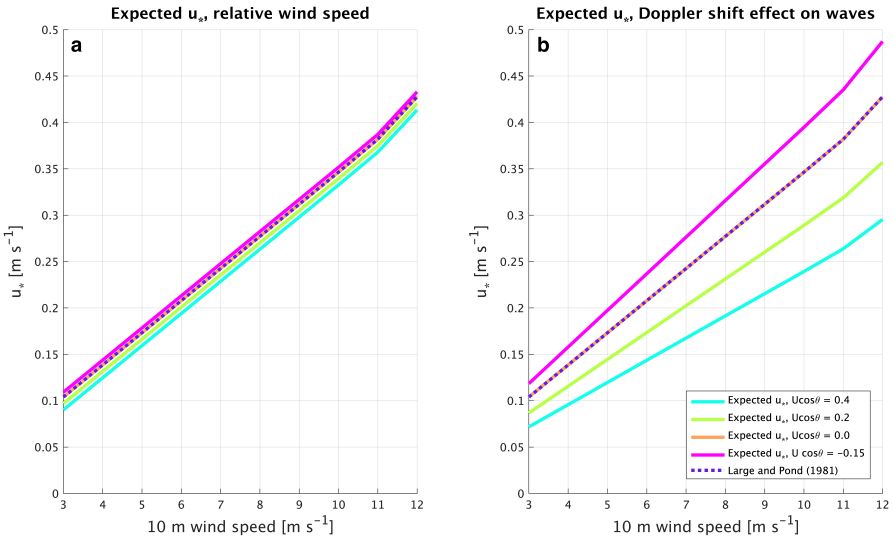

Figure 1. (a) Expected variation in u_* due to the direct effect of currents, assuming C_D from Large and Pond (1981) (current-relative wind, equation 2); (b) Expected variation in u_* due to the Doppler shift effect (wave-current interaction, equations 5,8).

et al., 2016; Zippel & Thomson, 2017; Gemmrich & Pawlowicz, 2020), the influence of wave-current interactions on u_* has not been explored in the open ocean using observations, with the exception of areas with strong mesoscale activity and current variations (Holthuijsen & Tolman, 1991; Romero et al., 2017; Hegermiller et al., 2019). The theory suggests that even small changes in surface currents will have non-negligible effects on u_* (Figure 1b), so wave-current interactions may still be important in locations away from coastal areas or major western boundary currents. Furthermore, areas without strong mesoscale activity are more representative of the global ocean as a whole. A goal of the present study is to evaluate the impact of wave-current interactions in a region of moderate mesoscale activity (Figure 2).

2 Methods

2.1 Study site

The NOAA Atlantic Tradewind Ocean-atmosphere Mesoscale Interaction Campaign (ATOMIC), part of EUREC^{4}A (Stevens et al., 2021), took place in January-February 2020 in the northwestern tropical Atlantic, east-northeast of Barbados (Figure 2). This region is north of the inter-tropical convergence zone and well within the trade wind region. As a result, wind and waves are typically strong and westward following the prevailing trade winds, with minimal directional variation. The ATOMIC study site is also adjacent to a region that has strong oceanic mesoscale activity (Figure 2) and spatial variability in ocean temperature and salinity: The outflows of the Amazon and Orinoco Rivers are nearby and large mesoscale ocean eddies are generated by the North Brazil Current (Fratantoni & Glickson, 2002; Ffield, 2005; Fratantoni & Richardson, 2006). Despite this, only moderate eddy kinetic energy was observed during the field campaign (Figure 2) because the study site is farther north than the region of highest eddy kinetic energy and freshwater discharge (Reverdin et al., 2021) and the field campaign took place before the boreal spring peak in discharge (Coles et al., 2013). However, river outflow

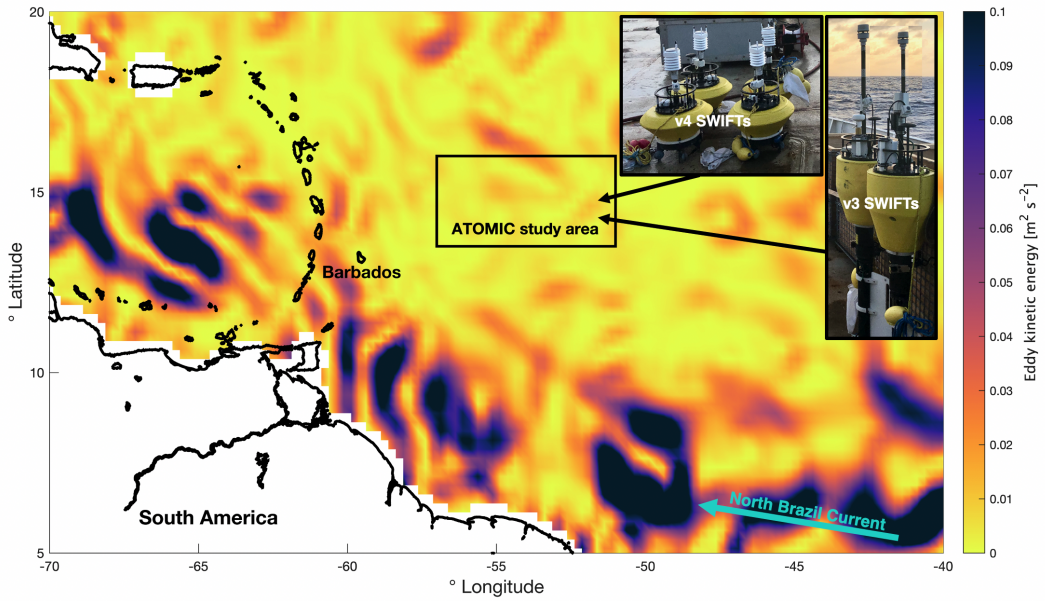

Figure 2. Eddy kinetic energy calculated from Copernicus Marine Environment Monitoring Service (CMEMS) satellite sea level anomalies on February 1, 2020. The rectangular box denotes the study area where SWIFTs were deployed and recovered. Inset images picture the two types of SWIFTs deployed during ATOMIC.

or mesoscale eddies are still likely responsible for the observed submesoscale spatial variability in the ATOMIC study area (Figure 2).

2.2 SWIFT observations

During the ATOMIC field campaign, two version 3 (v3) Surface Wave Instrument Float with Tracking (SWIFT) drifters (Thomson, 2012) and four version 4 (v4) SWIFT drifters (Thomson et al., 2019) were deployed. The field campaign consisted of two cruise legs on the NOAA Ship Ronald H. Brown (Quinn et al., 2021) and eleven NOAA P-3 aircraft flights (Pincus et al., 2021) from Barbados to the study area shown in Figure 2. SWIFT drifters were deployed twice from the NOAA Ship Ronald H. Brown: from 14 Jan 2020 to 22 Jan 2020 during Leg 1 and from 30 Jan 2020 to 11 Feb 2020 during Leg 2. Leg 1 deployments were made in the northeastern part of the study area, and Leg 2 deployments were made in the southwestern part of the study area. Details of these deployments and other measurements that were made during ATOMIC from the NOAA Ship Ronald H. Brown or other oceanic platforms are included in Quinn et al. (2021).

During both legs of ATOMIC, ocean temperature fronts were identified using satellite measurements and shipboard sensors. SWIFTs were then strategically deployed in a line across the front, with 5-10 km spacing between each drifter's initial deployment position. This strategy ensured that significant spatial variability in ocean temperature and surface currents was observed during the beginning of each deployment. Towards the end of deployments, SWIFT drifters converged to one (leg 1) or two (leg 2) general geographic areas due to currents.

V3 and v4 SWIFTs differed in height and had instrumentation at different heights and depths. V4 SWIFTs were equipped with Vaisala WXT350 meteorological sensors at 0.5 m height, which measured parameters including air temperature, relative humidity, and wind speed and direction. V3 SWIFTs were equipped with Airmar 200WX me-

teorological sensors at 0.8 m height, which measured the above parameters excluding relative humidity. Aanderaa 4319 sensors measured conductivity and ocean temperature at 0.3 m depth on v4 SWIFTs and at 0.5 m and 1.0 m on v3 SWIFTs. A downlooking pulse-coherent Nortek Aquadopp ADCP measured high-resolution vertical profiles of velocity that were used to estimate turbulent kinetic energy dissipation rates from one of the v3 SWIFTs using the second-order structure function of velocity profiles (Wiles et al., 2006; Thomson, 2012). Nortek Signature 1000 (v4) or Nortek Aquadopp (v3) ADCPs measured ocean current velocities below 0.5 m. Directional wave spectra and bulk wave parameters were estimated from inertial motion observations on both v3 and v4 SWIFTs using a Microstrain 3DM-GX3-35 (v3) or SBG Ellipse (v4) attitude and heading reference system (AHRS). These systems also included GPS measurements, with wave spectral processing as described in Thomson et al. (2018). Raw data were processed onboard, and spectral results were sent via Iridium telemetry once per hour, corresponding to a 10 minute burst of raw data at the top of each hour.

2.3 Data processing

Offsets in wind speed measurements were calibrated using shipboard observations made when a drifter was within 5 km of the ship by assuming that ship and drifter observations should be identical and performing linear regressions for each platform (Thomson et al., 2021). If fewer than 5 collocated data points were available for a given regression, offsets were first corrected using observations from another drifter that was near the ship. For one v4 drifter, a distance limit of 15 km was used because of a lack of data from other drifters closer than that. Root mean square errors in offsets were generally lower than sensor precision specifications; wind speed observations from individual SWIFTs had uncertainties between 0.24 and 0.96 ms^{-1}.

SWIFT drifters are nearly Lagrangian, surface-following platforms (Thomson, 2012), which drift with the surface currents. Surface currents are estimated from the drift track of SWIFTs after subtracting the contribution from Stokes drift following the methods of Thomson et al. (2019). These Stokes corrections are small (cms^{-1}) relative to the surface currents. mss and equilibrium u_* are calculated from wave spectra, assuming a constant equilibrium frequency range over which the source and sink of wave energy is balanced (equations 3 and 4). (Thomson et al., 2013) define the equilibrium frequency range as between 0.2 and 0.4 s^{-1}. We slightly modify this range and use $f_{min} = 0.25\ s^{-1}$ and $f_{max} = 0.4\ s^{-1}$ since since swell is occasionally observed at frequencies between 0.2 and 0.25 s^{-1}. Linear fits to the equilibrium range of the spectra in log-log space have an average slope of -3.89 (Figure 3a,c), roughly consistent with the theoretical f^{-4} shape. Minor deviations from the f^{-4} shape are frequently observed, although spectral slopes in the equilibrium range are rarely less steep than f^{-3} or steeper than f^{-5} (Figure 3c). Deviations from the f^{-4} shape are likely due to noise combined with the limited amount of data (10 minutes) used to calculate each spectrum.

Spectral shapes at high frequencies may be modulated by swell waves (Vincent et al., 2019) or coupling between the swell and high frequencies (Collins et al., 2018); when swell is strong (high wave centroid periods), spectral slopes are typically steeper than f^{-4} (Figure 3c). The transition between the equilibrium (f^{-4}) and saturation (f^{-5}) subranges has also been shown to be shifted to lower frequencies when u_* is high (Lenain & Melville, 2017). Sensitivity tests involving calculating mss and equilibrium u_* using an equilibrium frequency range prescribed based on the wave peak frequency (i.e., as done by Banner, 1990), centroid frequency, or wave age produce results negligibly different from the above method (not shown). Removing spectra with significant deviations from the f^{-4} shape (Figure 3c) also has minimal influence on the overall results. To remove dependence on the selected equilibrium range, mss is normalized by the constant equilibrium range frequency width of 0.15 s^{-1} (i.e., dividing mss calculated from equation 4

by f_{max} - f_{min}). Hereinafter, mss will refer to the frequency-width-normalized value rather than the unnormalized value.

Wave directions are calculated using directional moments and the maximum entropy method (Lygre & Krogstad, 1986). For consistency with the mss observations, the averaged value in the equilibrium range is used as the wave direction. An energy-weighted average direction was also calculated, but rarely differed by more than 10°from the average direction and thus was not used. mss, equilibrium u_*, and wave direction data are smoothed over 3-hour periods because each individual spectrum consists of only 10 minutes of data (12 degrees of freedom), which is not enough to obtain robust estimates of wave parameters. For consistency, all other atmospheric and oceanic observations are smoothed over 3-hour periods. In general, when winds are higher, waves are more energetic (Figure 3a). This leads to greater mss (equation 4). An objective of the present study is to isolate the dominant effect of wind speed on spectral energy in order to evaluate a secondary effect, in which opposing or following surface currents influence spectra and mss through wave-current interactions.

Data collected during a large swell event that occurred from 19-21 Jan 2020 are excluded from further analysis because of the effect of swell waves on the wave directional spectra in the equilibrium range. First, when swell is strong, high frequency wave directions are shifted away from the wind direction, leading to a much larger directional spread. Because wave energy is spread over a wide directional range, it is difficult to determine the direction aligned with the currents that would be expected to be most significantly influenced by wave-current interactions. Second, swell is associated with elevated energy levels between 0.25 and 0.3 s^{-1}, which leads to spectral slopes that are consistently steeper than f^{-4} (Figure 3c) and therefore inconsistent with equilibrium theory. Swell modulation of the mid- to high-frequency portion of the wave spectrum, including shifting the transition frequency between the equilibrium and saturation subranges, has previously been observed (Vincent et al., 2019). To exclude conditions where swell significantly influenced high-frequency energy levels, we only analyze data where the average wave direction in the equilibrium range is $> 0°$and $< 150°$, as high frequency wave directions during the swell event were typically 150°to 300°. This criterion eliminates data almost exclusively from the 19-21 Jan 2020 swell event, which comprise <6% of all observations.

v3 SWIFTs are larger in size and much taller than v4 SWIFTs (Figure 2 inset) and thus susceptible to bias at high frequencies due to tilting at high wind speeds. To account for this, mss observations from each v3 SWIFT are corrected using data from v4 SWIFTs. This is done by comparing mss observations from v3 and v4 SWIFTs when a v4 SWIFT was within 20 km of the v3 SWIFT. Linear regressions of wind speed versus mss are then developed to relate v3 and nearby v4 data, and v3 data are corrected by subtracting the difference between the linear fits at each wind speed. On average, this correction decreases mss by 1.5×10^{-3}, or 6.2%, with slightly larger corrections at higher wind speeds. A sensitivity test that involved re-calculating mss and u_* without making this correction (not shown) determined that correcting the tilting bias has little effect on the results presented in subsequent sections.

Data processing techniques used to correct wind speed and v3 mss measurements involved using observations from closely spaced platforms to develop a linear relationship used to make corrections. Spatial variations likely exist on small scales, so observations from nearby drifters are not always equivalent for individual data pairs. However, this correction method is reasonable for several reasons: First, many pairs of drifters were much closer together than the stated criterion; for instance, v4 drifters used to correct mss from v3 drifters were only 10.8 km apart on average. Second, large amounts of data (n=598) are used to calculate the relationships used to correct v3 mss. Because of this, the spatial variability between drifters, a source of random error, is smoothed out when constructing regressions. Finally, in the individual case with significant spatial vari-

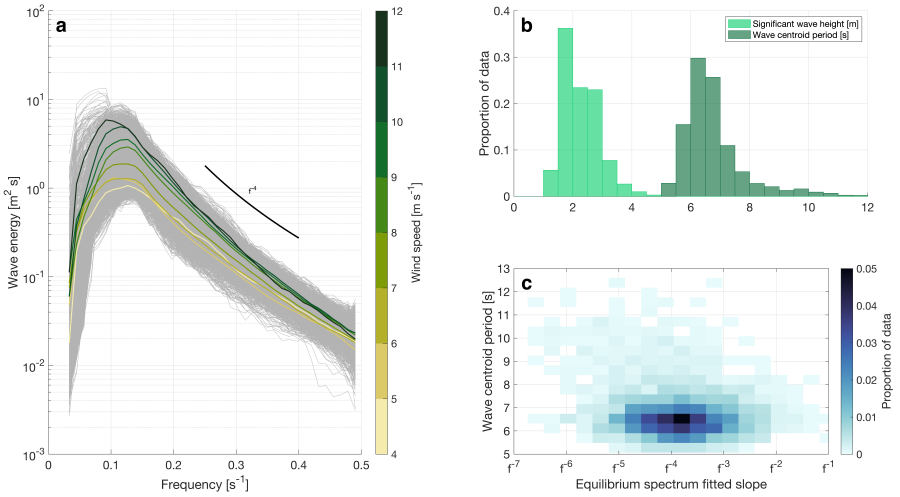

Figure 3. (a) Wave spectra observed from v4 SWIFT drifters during both legs of ATOMIC. Energy at individual frequencies was smoothed over a 3-hour time period and in frequency space over 0.059 s^{-1} (grey; n=1156). Colored lines denote average spectra within 1 ms^{-1}-wide wind speed categories. Spectra with a wave direction of $< 0°$or $> 150°$had significant swell input and are excluded. (b) Histograms of significant wave height and wave centroid period from all drifters. (c) Binned scatter plot of wave centroid period vs fitted equilibrium range spectral slope for all drifters.

ability highlighted in section 3.2.3, variability is on scales of over 20 km and hence a correction on smaller scales would not influence those results.

3 Results

We first evaluate the range of wind, wave, and current conditions observed during ATOMIC (section 3.1). We then evaluate how mss and equilibrium u_* differ across different current conditions in case studies on varying spatial scales (section 3.2) and collectively in the study area (section 3.3). Results are reported in section 3.2 in terms of mss to highlight the effect of wave current interactions on wave slope, while results are discussed in section 3.3 in terms of u_* to highlight the effects on friction velocity and air-sea momentum flux. We reiterate that reported mss and u_* are directly proportional and hence observations are essentially interchangeable: assuming $f_{max} - f_{min} = 0.15$ s^{-1}, $\beta = 0.012$, and $I(p) = 2.5$, u_* will be higher than mss by exactly a factor of 13.0 and higher than unnormalized mss by a factor of 86.7 (equation 5).

3.1 Wind, Wave, and Current Conditions during ATOMIC

Wind directions during ATOMIC were typically from the east or northeast following the prevailing trade winds. Wind speeds were variable: observed values ranged from 3.7 ms^{-1} to 13.0 ms^{-1} with a mean of 8.2 ms^{-1} and a standard deviation of 1.6 ms^{-1} (Figure 4d). Variations in wind speed led to variations in significant wave height. Significant wave heights averaged 2.3 m with a standard deviation of 0.6 m (Figure 3b), but were elevated to over 4 m during the swell event on 19-21 Jan 2021. Significant wave height was positively correlated with wave period; a mean wave centroid period of 6.8 s was observed, but this value increased to over 9 s during the swell event. As discussed previ-

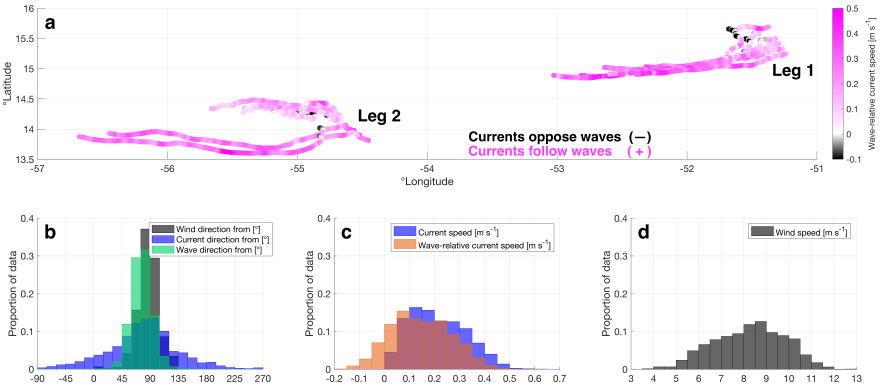

Figure 4. (a) Drift tracks of all SWIFT drifters during both legs of ATOMIC. Colors represent the component of the current vector aligned with the waves. Histograms of data from all drifters: (b) wind (v3 only), wave, and current direction; (c) current and wave-relative current speed; (d) wind speed

ously, we exclude data from this period. Wave directions in the equilibrium frequency range were within ±20° of the wind direction 78% of the time (Figure 4b). Surface ocean current directions were usually aligned with the wind and waves, but had significantly greater variability. Currents were westward and aligned (within ±90°) with the waves 89% of the time (Figure 4a-c). Currents opposed the waves (> |90°| angle between wind and wave directions) 11% of the time. Current speeds were on average 0.21 ms^{-1}, with a standard deviation of 0.11 ms^{-1}. The vector component of the current aligned with the waves (i.e., the wave-relative current) varied between -0.16 ms^{-1} and 0.57 ms^{-1}, with an average of 0.15 ms^{-1} and a standard deviation of 0.12 ms^{-1}. Wave-relative currents were between 0.0 and 0.3 ms^{-1} 75% of the time.

As discussed previously, SWIFT drifters are Lagrangian platforms which follow the surface currents. Drifters often made loops and turns due to current variability on timescales of under 24 hours. This is considerably shorter than the inertial period, so these features are likely fronts or filaments rather than inertial oscillations. Surface current variability is especially apparent during Leg 2: Currents were slower and highly variable in the northern region with four drifters, and faster and aligned with the wind in the southern region with two drifters (Figure 4a).

3.2 Case studies

3.2.1 Case 1: Small-scale current loop

Two SWIFTs drifted towards the southwest in the southern part of the study region for a 60 hour period from 0000 UTC on 2 February 2021 to 1200 UTC on 4 February 2021, during the second set of drifter deployments. During this period of time, the other four drifters were located about 70 km to the north. While the two drifters generally drifted southwestward, a 12-hour-long shift in current direction caused them to briefly drift eastward. This resulted in the observed loops, on the scale of a few km, in the drift tracks at 54.82°W in Figure 5a. Wind speeds steadily decreased from 9 to 4 ms^{-1} throughout most of the 60-hour period, though both wind and waves were consistently from the northeast without changing direction (Figure 5a). This is expected in a region

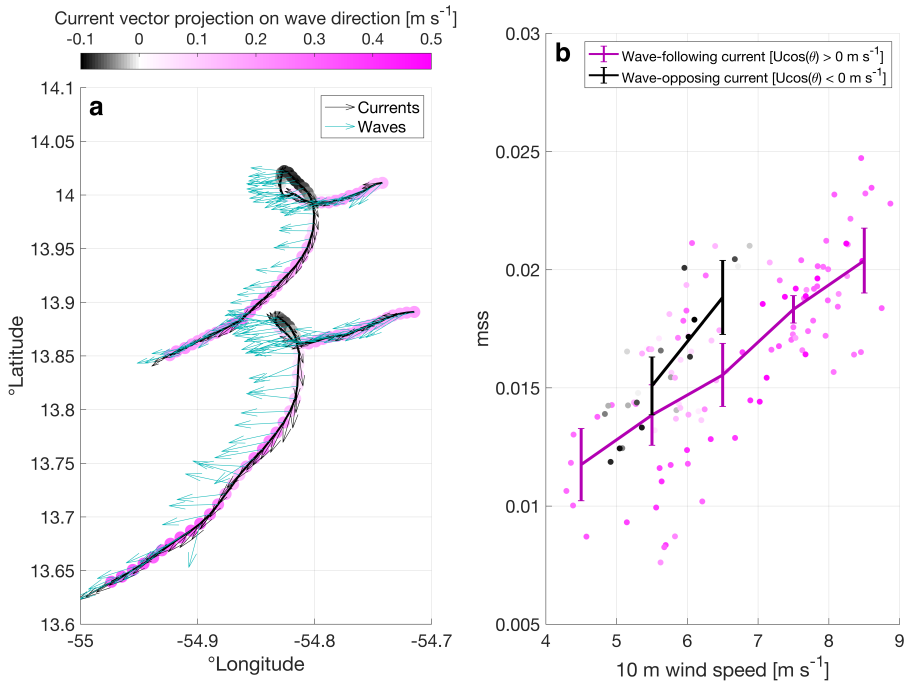

Figure 5. SWIFT observations from Case 1. (a) Drift tracks. Colors represent the component of the current vector aligned with the waves, black quivers represent the current direction, and cyan quivers represent the wave direction. (b) *mss* vs. wind speed for two SWIFT drifters from 2 Feb 2020 0000 UTC to 4 Feb 1200 UTC during leg 2 of ATOMIC. Lines denote averages in 1 ms^{-1}-wide wind speed bins, separated by the wave-relative current ($Ucos\theta$). All plotted bins contain a minimum of 5 data points.

with prevailing trade winds. Wind speeds were between 5 and 7 ms^{-1} during the loop and several hours afterward.

Because wind and wave directions were relatively constant, the 12-hour period of eastward currents corresponds to conditions where the currents and waves were in opposite directions, as seen by the black markers in Figure 5. When currents opposed waves, *mss* was considerably higher than when currents were aligned with the waves during similar wind conditions (Figure 5b). Specifically, average *mss* at wind speeds between 5 and 6 ms^{-1} was 9% higher in opposing current conditions. At wind speeds between 6 and 7 ms^{-1}, this difference was 21% and statistically significant at the 95% confidence level (Figure 5b). Currents opposing waves were not frequently observed outside of 5-7 ms^{-1} winds. The average difference in wave-relative current between the wave-following and wave-opposing conditions (pink and black lines in Figure 5b) was 0.22 ms^{-1}, which is expected to be associated with a difference in *mss* of 3.6% due to the difference in relative winds (Figure 1a). Thus the observed *mss* differed by a much greater amount between current regimes, suggesting that wave-current interactions elevated or suppressed wave slopes while the surface currents were opposing or following the waves.

3.2.2 Case 2: Submesoscale current reversal

Two SWIFTs made a clockwise reversing turn, on the scale of 10 km, during a 60 hour period from 1200 UTC on 2 February 2021 to 0000 UTC on 5 February 2021. These

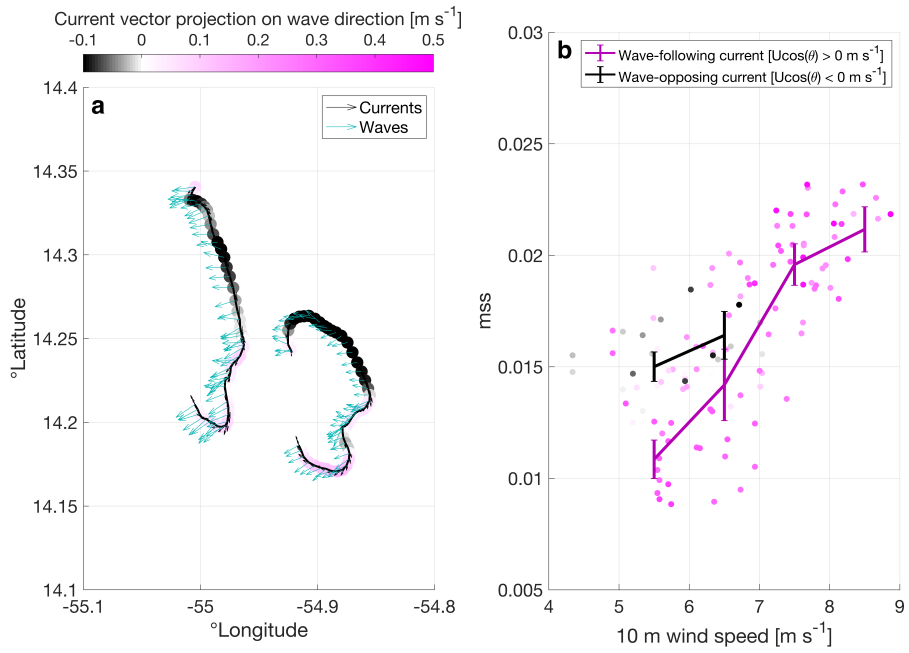

Figure 6. SWIFT observations from Case 2. (a) Drift tracks. Colors represent the component of the current vector aligned with the waves, black quivers represent the current direction, and cyan quivers represent the wave direction. (b) mss vs. wind speed for two SWIFT drifters from 2 Feb 2020 1200 UTC to 5 Feb 2020 0000 UTC during leg 2 of ATOMIC. Lines denote averages in 1 ms^{-1}-wide wind speed bins, separated by the wave-relative current ($Ucos\theta$). All plotted bins contain a minimum of 5 data points.

drifters, along with two other drifters (not shown), were in a northern area of cooler water pool. In this location, currents were slower and more variable compared to case 1. Wind speeds were roughly steady around 4-6 ms^{-1} for the first 36 hours, before increasing to 7-9 ms^{-1} for the remainder of the time period. Wind and wave directions were consistently from the east (Figure 6a).

Surface current direction varied significantly over the 60-hour time period. While winds were light (< 7 ms^{-1}), surface currents initially opposed waves for 20 hours, as evidenced by the southeastward drift of the SWIFTs, before turning westward. Once winds increased to over 7 ms^{-1}, surface currents generally followed the wind and waves. At low wind speeds, mss was significantly elevated when currents opposed waves (Figure 6b). For instance, at winds of 5-6 ms^{-1}, average mss was 38% higher when currents opposed waves. Similar to the previous case study, this suggests that wave-current interactions elevated mss when currents and waves were misaligned. The larger spatial and longer time scales of this case, compared to case 1, are indicative of a submesoscale ocean feature.

3.2.3 Case 3: 30-50 km front

Three SWIFTs drifted southwestward during a 48-hour period from 15 Jan 2020 0800 UTC to 17 Jan 2020 0800 UTC near the start of leg 1 of ATOMIC. A ocean temperature front existed between the southernmost and two northern drifters, as evidenced by a spatial difference in ocean temperature of about 0.3°C (Figure 7c) across 30-50 km.

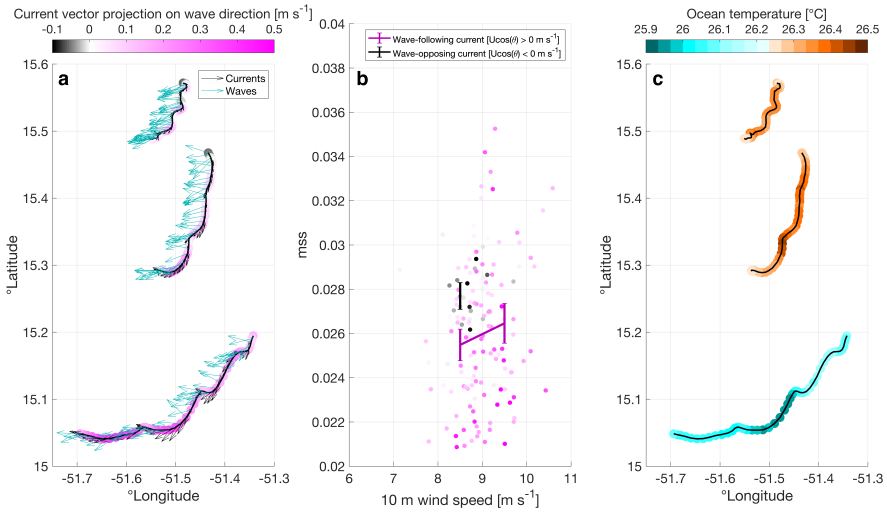

Figure 7. SWIFT observations from Case 3. (a) Drift tracks. Colors represent the component of the current vector aligned with the waves, black quivers represent the current direction, and cyan quivers represent the wave direction. (b) mss vs. wind speed for two SWIFT drifters from 15 Jan 2020 0800 UTC to 17 Jan 0800 UTC during leg 2 of ATOMIC. Lines denote averages in 1 ms^{-1}-wide wind speed bins, separated by the wave-relative current ($Ucos\theta$). All plotted bins contain a minimum of 5 data points. (c) Drift tracks. Colors represent near-surface ocean temperature in the top 0.5 m.

Currents were also considerably faster south of the front, as seen by the long drift track of the southernmost drifter (Figure 7a). Unlike the previous two case studies, wind speeds were steady at 8-10 ms^{-1} throughout the domain (Figure 7b).

Because wind speeds were generally invariant, we evaluate the variability in mss using histograms of wind speed, wave-relative current, mss, and ocean temperature in three wave-relative current regimes: strong and weak wave-following currents and wave-opposing currents (Figure 8). A threshold of 0.2 ms^{-1} is chosen to separate strong and weak wave-following currents, so that data are relatively evenly distributed between those two categories. Wind speeds were, on average, slightly higher when currents strongly followed the waves (Figure 8i). Despite the stronger winds, mss was considerably lower in these wave-following current conditions (Figure 8k). On the other hand, mss was relatively high, never falling below 2.5×10^{-2}, when currents opposed the waves (Figure 8c). These results demonstrate that in this case with nearly invariant winds, wave-relative currents were the primary driver in modulating mss. The near-surface ocean temperatures associated with current regimes (Figures 7c, 8d,h,l) show that strong following wave-relative currents (> 0.2 ms^{-1}) were almost exclusively observed south of the temperature front, while weaker following and opposing wave-relative currents were almost exclusively observed by the northern two drifters. These results suggest that the mesoscale temperature front coincided with a front in surface currents that led to spatial variability in wave-current interactions. While existing studies have demonstrated that wave-current interactions drive spatial variability across fronts in the coastal ocean (e.g., Thomson et al., 2014; Gemmrich & Pawlowicz, 2020, and others), this effect has not previously been shown in open ocean observations outside of areas with strong current activity, to our knowledge.

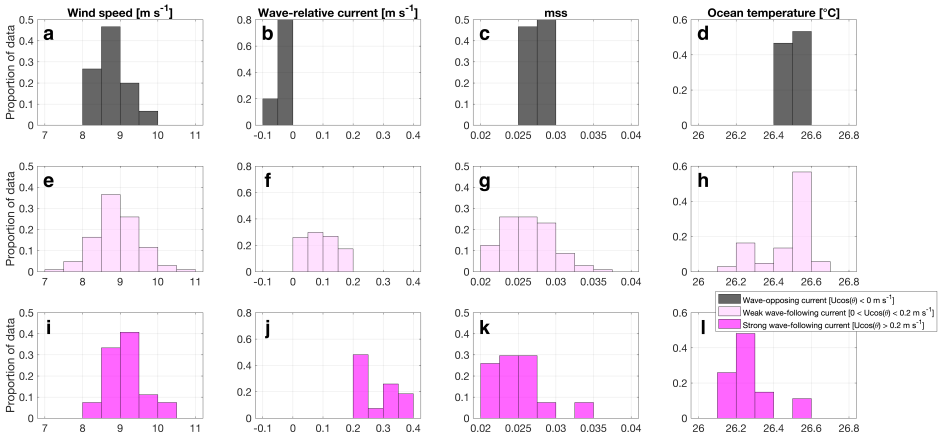

Figure 8. Histograms of SWIFT observations from Case 3: (a,e,i) wind speed, (b,f,j) wave-relative current, (c,g,k) mss, and (d,h,l) ocean temperature for three SWIFT drifters from 15 Jan 2020 0800 UTC to 17 Jan 0800 UTC during leg 1 of ATOMIC. Colors represent categories of the wave-relative current: black denotes wave-opposing currents ($Ucos\theta < 0.0\ ms^{-1}$), light pink denotes weak wave-following currents ($0.0 < Ucos\theta < 0.2\ ms^{-1}$), and magenta denotes strong wave-following currents ($Ucos\theta > 0.2\ ms^{-1}$).

3.3 Synthesis of all data

Figure 9 shows the average observed mss and u_*, computed from equation 3 using the equilibrium range of the wave spectra, binned by wind speed and separated by wave-relative current conditions for all SWIFT observations during ATOMIC. u_* derived from wave spectra is generally consistent with the expected values of Large and Pond (1981). This suggests that wind speed and surface stress can be predicted from wave spectra alone and supports the findings of Voermans et al. (2020). At all observed wind speeds, u_* increases as wave-relative currents decrease (i.e., currents are more wave-opposing), although the differences are not always statistically significant at the 95% level. The variability in u_* between different current conditions generally increases with increasing wind speed, which is consistent with the theoretical predictions based on the Doppler shift effect shown in Figure 1b and equation 8. There are differences in u_* between different levels of wave-following currents, which suggests that wave-current interactions may be important even when wave-opposing currents are not present. At wind speeds above 9 ms^{-1}, the spread in u_* is smaller across current conditions than at slightly lower wind speeds. This contradicts the expectations shown in Figure 1, and may be a result of unsteady winds. That is, the wave field did not have sufficient time to respond to rapid variations in wind speed when winds were high.

To quantify the effect of wave-current interactions, it is necessary to isolate the effect of currents from the dominant effect of wind speed on u_*. A multiple linear regression assesses the variability in u_* independent of wind speed: assuming u_* depends only on wind speed and wave-relative current, the effect of currents and wind speed on u_* can be individually quantified. This regression is described by Equation 9,

$$u_* = x + y\ U_{10} - z\ Ucos(\theta), \tag{9}$$

which shows the average individual contributions of wind speed (U_{10}) and wave-relative current ($Ucos(\theta)$) to u_*. Using u_* inferred from the wave spectra and U_{10} and $Ucos(\theta)$

from the SWIFT observations, we find that $x = -0.043 \pm 0.006$ (standard error), $y = 0.042 \pm 0.001$, and $z = -0.077 \pm 0.009$ ($R^2 = 0.66$). Physically, y and z are the contributions of U_{10} and $Ucos(\theta)$ to u_*. The offset x is likely an artifact of the differences between the moderate- and low-wind relationship between U_{10} and u_* (Edson et al., 2013), with additional contribution from the assumption of constant β and $I(p)$ in calculations of u_*. This relation demonstrates that the variation in u_* across different current conditions is greater than what is expected from the current-relative wind alone. That is, the observed spread in u_* (Figure 9) is greater than the prediction shown in Figure 1a. A wave-relative current change of 0.1 ms^{-1} was, on average, associated with a change of 0.0077 ms^{-1} in u_* (compared to 0.0035 ms^{-1} expected from equation 2 and Figure 1a). Equation 9 suggests that the range of observed values of wave-relative current of approximately 0.7 ms^{-1} will lead to variations in mss and u_* of 18%, at moderate wind speeds of 8-9 ms^{-1} (compared to 8% expected from equation 2 and Figure 1a). Another method of quantifying the influence of surface currents on u_* is to calculate the difference between the observed u_* and predicted value from the Large and Pond (1981) relationship, which doesn't incorporate wave effects, and determine a relationship between this residual u_* and the wave-relative current. This analysis yielded similar results as the multiple linear regression, with a slightly smaller dependence of wave-relative current on u_*: residual u_* decreased by 0.0057 ms^{-1} for every 0.1 ms^{-1} increase in wave-relative current. These analyses demonstrate that in the ATOMIC study area, which has consistent and strong wave-following currents, u_* and mss may be significantly increased or decreased due to wave steepening or flattening from wave-current interactions. This is likely also applicable to other regions of the ocean with similar wind speeds and moderate current variability.

These findings support the hypothesis that wave-current interactions in the open ocean significantly modify u_* when currents strongly follow or oppose the waves. However, the overall variation in observed u_* is less than the expected spread for a single theoretical wave after applying a Doppler shift; i.e., lines are spaced farther apart in Figure 1b than in Figure 9. We expect that this discrepancy is primarily due to the directional spread of waves. Calculated from directional moments obtained from SWIFT onboard processing, average wave directional spread in the equilibrium frequency range is around 45°, with typical fluctuations up to 20°. The spread may partially result from scattering effects from submesoscale current velocity variations (Smit & Janssen, 2019), which were commonly observed in this area. The large wave directional spread indicates that a significant portion of the wave spectrum will not be directly aligned with the surface currents when the surface currents oppose or follow the average wave direction. Thus, the net effect of currents on wave steepening or flattening will be lower than expected for a single theoretical wave. The assumption of a constant $I(p)$ in the calculation of u_* (equation 3) may also have contributed to the weaker signal, as directional spreading may co-vary with the alignment and direction of the waves. In addition, nonlinear interactions and contributions from the lower frequency portion of the spectrum (Vincent et al., 2019) may have smoothed out differences in u_* between current regimes.

To assess the contribution of wave-current interactions to air-sea momentum flux, we calculate momentum flux from equilibrium u_* and ρ_a observations using equation 1. The physical idea is the mss is a proxy for surface roughness, and that is directly related to the wind friction velocity and the momentum flux. ρ_a was determined from air temperature, air pressure, and relative humidity observations on the v4 SWIFTs. Because relative humidity observations were not available from the v3 SWIFTs, meteorological observations made on the NOAA Ship Ronald H. Brown (Thompson et al., 2021) were used to estimate ρ_a for these drifters. This approximation had a negligible effect, as ρ_a varied minimally (mean ρ_a on the ship was 1.172 $kg\ m^{-3}$ with a standard deviation of 0.003 $kg\ m^{-3}$). Momentum flux calculated using u_* from wave spectra and equation 1 will hereinafter be referred to as τ_{waves}. We note that using τ_{waves} as a measure of momentum flux is contingent on the assumption that wind-wave equilibrium is valid and

spectra follow the theoretical f^{-4} shape; see section 4.3 for a discussion. Figure 10a compares wind speed and τ_{waves}: τ_{waves} varies significantly between current conditions for a given wind speed. These differences are statistically significant at moderate wind speeds of 7 to 9 ms^{-1} commonly observed during ATOMIC. Equation 10,

$$\tau_{waves} = X + Y\ U_{10} - Z\ Ucos(\theta), \tag{10}$$

represents the dependence of τ_{waves} on wind speed and wave-relative current. Performing a multiple linear regression, we find that $X = -0.116 \pm 0.004$ (standard error), $Y = 0.028 \pm 0.001$, and $Z = -0.057 \pm 0.007$ ($R^2 = 0.61$). Similar to Equation 9, X is an offset and Y and Z are the contributions of U_{10} and $Ucos(\theta)$ to τ_{waves}. τ_{waves} varies by 0.0057 Nm^{-2} on average for a 0.1 ms^{-1} change in wave-relative current. Across the entire 0.7 ms^{-1} range of observed wave-relative currents, τ_{waves} is expected to vary by 37% at moderate wind speeds of 8-9 ms^{-1} (equation 10). This variation is comparable to the change in momentum flux that would be associated with a wind increase or decrease of 3 ms^{-1}, according to the Large and Pond (1981) relationship.

Previous studies have shown that wave statistics, including mss, are improved when spectra are normalized by the wave directional spread (Banner et al., 2002; Schwendeman & Thomson, 2015). We recalculated mss from the wave spectra after normalizing spectra by the directional spread ($\Delta\theta$), in addition to the aforementioned normalization by the equilibrium frequency range width: normalizing by $\Delta\theta$ had a minimal effect on the magnitude of mss; however, it increased the spread in mss between different wave-relative current conditions slightly (not shown). Normalizing by $\Delta\theta_2$, the directional spread calculated with the second-order moments of the wave spectra (Thomson et al., 2018), increased the magnitude of mss but did not affect the spread in mss between different current conditions. In short, variance in mss across different wave-relative current conditions exists whether or not spectra are normalized by $\Delta\theta$ or $\Delta\theta_2$. Hence, mss only normalized by the frequency width are shown.

4 Discussion and Conclusions

4.1 Wave-breaking turbulence

Surface currents modify wave slope depending on the alignment of the currents relative to the wave direction. By extension, wave-current interactions are expected to influence near-surface turbulence: If waves are steeper, more wave breaking would be expected to enhance near-surface turbulent kinetic energy (TKE) dissipation rates (e.g., Agrawal et al., 1992; Craig & Banner, 1994; Terray et al., 1996; Thomson, 2012, and others). TKE dissipation rates were estimated using the second-order structure function of high-resolution velocity profiles (Wiles et al., 2006; Thomson, 2012) collected with the ADCP on SWIFT 17, one of the v3 SWIFT drifters (dissipation data from other drifters are not available). Figure 11 shows that TKE dissipation rate, as expected, is positively correlated with wind speed. Wave-current interactions appear to have a weak but discernible influence on dissipation rates: at moderate wind speeds between 6 and 9 ms^{-1}, depth-averaged dissipation rates in the top 22 cm are elevated when currents oppose waves. Because each bin contains a limited amount of data, this difference is only statistically significant at 8-9 ms^{-1}. At wind speeds under 6 ms^{-1}, dissipation rates are statistically similar between wave-opposing and wave-following current conditions. While these findings suggest that wave-relative currents influence near-surface turbulence, the relationship is not strong. We infer that the lack of a clear relationship between wave-relative currents and dissipation rate is due to two factors. First, only a limited amount of dissipation data were collected during ATOMIC, and those data are from a single drifter. Second, wave breaking-enhanced turbulence is intermittent (Derakhti et al., 2020), so the 10-minute segments of data collected during ATOMIC may not capture small dissipation rate increases or decreases resulting from the roughly 10% changes in wave slope

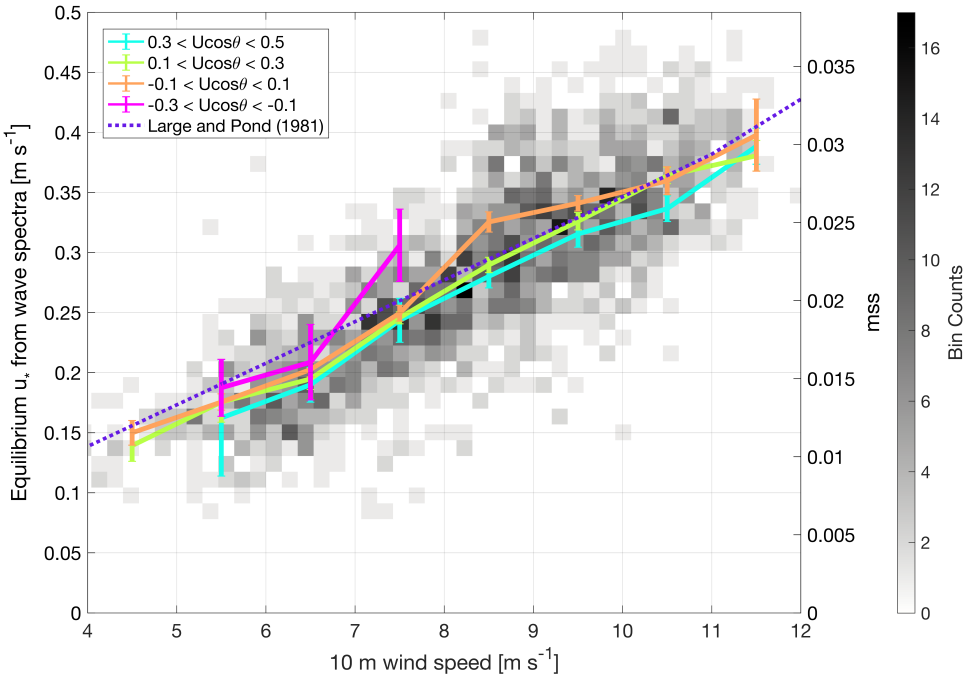

Figure 9. Wind speed vs. equilibrium u_* and mss for all SWIFT data during both legs of ATOMIC. Lines denote averages in 1 ms^{-1}-wide wind speed bins, colored by the wave-relative current ($Ucos\theta$). Error bars represent 95% confidence intervals around the mean of each bin. Grey shading represents the number of observations near a given wind speed and mss or u_*. All plotted bins contain a minimum of 5 data points. The dotted purple line shows expected values of u_* calculated from the relationship in Large and Pond (1981).

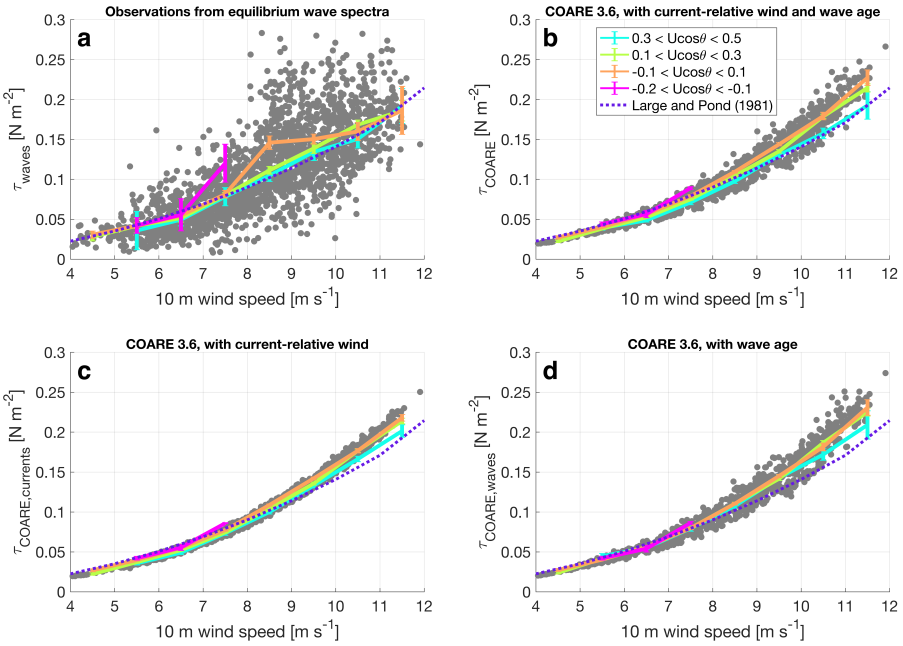

Figure 10. Momentum flux vs. wind speed calculated from (a) equilibrium u_* inferred from wave spectra for all SWIFT data and (b-d) version 3.6 of the COARE algorithm for v4 SWIFT data, during both legs of ATOMIC. COARE 3.6 inputs included (b) observed surface currents and waves, (c) observed surface currents but not waves, and (d) observed waves but not surface currents. Lines denote averages in 1 ms^{-1}-wide wind speed bins, colored by the wave-relative current ($Ucos\theta$). Error bars represent 95% confidence intervals around the mean of each bin. All plotted bins contain a minimum of 5 data points. Grey points represent wind speed and momentum flux observations, smoothed over a 3-hour period. The dotted purple line shows expected values calculated using Equation 1, with u_* determined by the relationship in Large and Pond (1981) and using the mean ρ_a observed by the Ronald H. Brown.

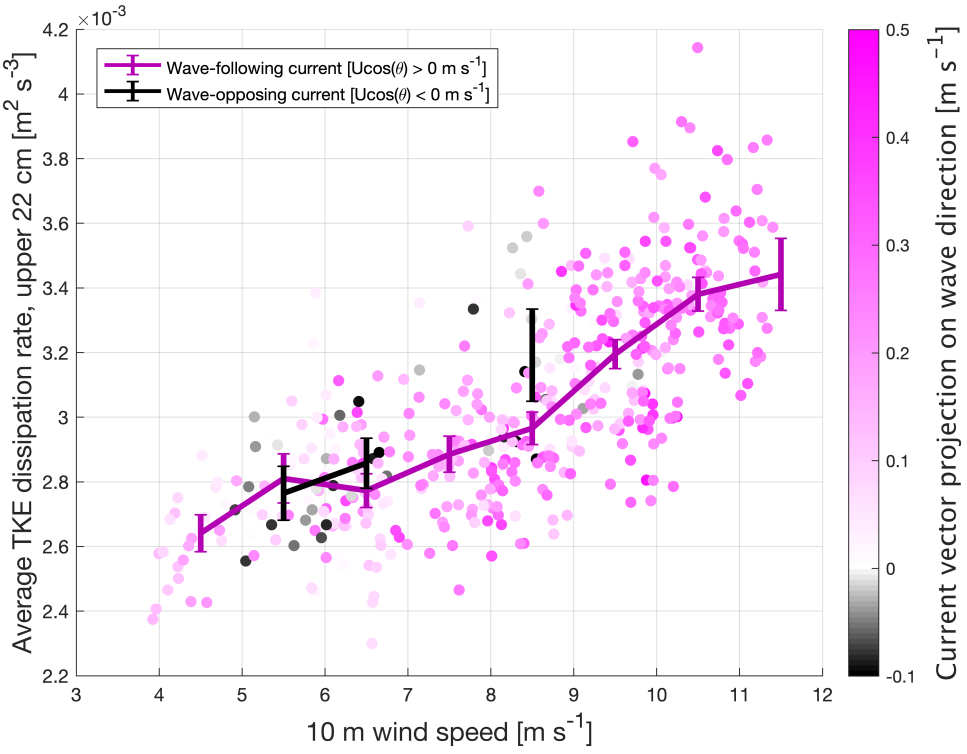

Figure 11. TKE dissipation rate (depth-averaged in the top 22 cm) vs. wind speed observed by SWIFT 17 during both legs of ATOMIC. Lines denote averages in 1 ms^{-1}-wide wind speed bins, separated by the wave-relative current ($Ucos\theta$). All plotted bins contain a minimum of 5 data points.

and subsequent wave breaking variations. Additional observations would be needed to clearly define this relationship.

4.2 Temporal and lateral variations in surface currents

The SWIFT observations demonstrate that both temporal and spatial variations in currents exist in the trade wind region encompassing the ATOMIC study area. For instance, case studies 1 and 2 (Figures 5,6) show variations in current speed and direction owing to a combination of increasing or decreasing wind speeds and larger-scale ocean variability, which modified currents throughout the area where drifters were deployed. That is, all drifters observed similar surface current speed and direction at a given time. On the other hand, case study 3 (Figure 7) exhibited spatial variations in surface currents, as winds were relatively steady throughout the domain but current speed and direction varied between drifters; i.e., drifters at different locations did not observe similar surface currents at the same point in time. This implies that there is lateral shear in surface currents, which presumably drives lateral variability in waves and air-sea fluxes. For instance, at 1200 UTC on 15 January 2020 near the beginning of case study 3, the southern two drifters are roughly 30 km apart, with wave-relative currents 0.13 ms^{-1} higher (more wave-following) at the location of the southernmost drifter (Figure 7). u_*, and τ_{waves} are 0.060 ms^{-1} and 0.043 Nm^{-2} larger at the location of the central drifter (not shown). This implies that an average lateral wave-relative current shear of just under 0.005 $ms^{-1}km^{-1}$ is responsible for average lateral variations of 0.002 $ms^{-1}km^{-1}$ and

615 $0.0015\ Nm^{-2}$ in u_* and τ_{waves}. These are significant variations which suggest that, along
616 with temporal current variability highlighted in cases 1 and 2, spatial variations of wave-
617 current interactions are a major source of uncertainty in studies assuming that currents
618 are uniform on submesoscales or mesoscales. That is, surface currents influence mss, u_*,
619 and momentum flux both when currents are spatially variable and when currents are spa-
620 tially homogeneous but temporally variable.

621 **4.3 Applications to air-sea fluxes**

622 The latest version (3.6) of the widely-used Coupled Ocean-Atmosphere Response
623 Experiment (COARE) bulk flux algorithm (Fairall et al., 2003; Edson et al., 2013) uti-
624 lizes a wave model (Banner & Morison, 2010) to parameterize the effect of wave age on
625 surface roughness and stress through the dominant wave phase speed (i.e., speed at the
626 spectral peak), significant wave height, and wind speed, but does not consider the effects
627 of surface currents on waves other than through changes in the current-relative wind speed
628 (equation 2). Because the results from section 3 indicate that wave-current interactions
629 significantly modulate momentum flux, we compare COARE 3.6 output, including and
630 excluding parameterizations of the current-relative wind and wave age, to observations
631 to evaluate the significance of wave-current interactions in modulating fluxes and gain
632 insight into the effectiveness of COARE 3.6 parameterizations of momentum flux when
633 surface currents are variable.

634 Momentum flux calculated using the COARE algorithm (τ_{COARE}), wind speed,
635 surface current, and wave conditions observed by the SWIFTs and other atmospheric
636 conditions observed at the Ronald H. Brown, is shown in Figure 10b. Figure 10c shows
637 momentum flux calculated using COARE 3.6 and prescribing observed surface currents
638 but not waves (i.e., identical to 10b except without wave height and peak period pre-
639 scribed as an input). Figure 10d shows momentum flux calculated using COARE 3.6 and
640 prescribing observed wave conditions but not surface currents. Wave phase speeds in-
641 put into COARE were calculated from the observed wave peak period and deep-water
642 wave dispersion relation. Even though centroid period is a more stable parameter that
643 is independent of the frequency spacing of the spectra, we use peak period as the dom-
644 inant wave period input into COARE because the current version of the COARE algo-
645 rithm was developed using peak period. v3 and v4 SWIFT peak periods are inconsis-
646 tent because of the tilting bias discussed earlier, so only v4 SWIFT data were used to
647 calculate momentum flux using COARE.

648 Figures 10b-d indicate that the variability of τ_{COARE} at a given wind speed is due
649 to both variations in current-relative wind (Figure 10c) and wave age (Figure 10d). There
650 is a larger difference between current conditions when only current-relative wind is pre-
651 scribed (Figure 10c) than when just wave age is prescribed (Figure 10d), indicating that
652 spread in τ_{COARE} between different wave-relative current conditions (Figure 10b) is largely
653 the result of current-relative wind variations rather than waves. The variations in τ are
654 much larger in the observations (gray points in Figure 10a) than in COARE (gray points
655 in Figure 10b), because COARE represents the mean stress observed under given con-
656 ditions and does not capture turbulent fluctuations inherent in the real world. However,
657 the variability in average τ between current conditions estimated using COARE (spread
658 between lines in Figure 10b) is also much smaller than in the observations (spread be-
659 tween lines in Figure 10a). For instance, at typical wind speeds of 8-9 ms^{-1}, τ_{waves} varies
660 by over 0.04 Nm^{-2} across current conditions (Figure 10a), while τ_{COARE} only varies by
661 roughly 0.01 Nm^{-2} (Figure 10b); i.e., τ_{waves} varies by up to 40% while τ_{COARE} varies
662 by only 10%. This implies that air-sea flux studies that only incorporate current-relative
663 winds but do not incorporate wave-current interactions (as done by wave age in COARE)
664 will not represent variations in momentum flux of up to 30% ($\pm$15%) at moderate wind
665 speeds and wave conditions.

Wave-current interactions also likely have an important role in the spatial variations in sensible, latent, buoyancy, and net heat fluxes, which are influenced by momentum flux. Assuming standard bulk flux relationships between τ, C_D, the transfer coefficients of heat and moisture, and the surface heat flux (as shown in Fairall et al., 1996) and assuming that only surface stress is modified and other terms remain the same, a 30% error in bulk momentum flux will lead to an error of approximately 14%, or 27 Wm^{-2}, of the air-sea sensible plus latent heat flux under average conditions observed during ATOMIC. As mentioned in section 3.3, a direct comparison between τ_{waves} and direct or parameterized flux estimates (i.e., τ_{COARE}) requires assuming that wave spectra used in the calculation of τ_{waves} follow a f^{-4} shape and wind and waves are in equilibrium. Time- and frequency-averaged spectra had a slope close to f^{-4} (Figure 3a,c), although small deviations from the expected f^{-4} shape occurred in a considerable number of spectra. Regardless, mss calculated from the spectra (directly proportional to u_* used to calculate τ_{waves}, as seen in equation 5) are indicative of the surface roughness and thus will modulate air-sea momentum fluxes, even if wind-wave equilibrium is not strictly satisfied.

Wind directions are relatively invariant in the ATOMIC study area. Many other areas of the world ocean have similarly consistent wind directions, including the tropics and midlatitudes with prevailing trade winds and westerlies, respectively. Because of this, the significant influence of current variability on waves and momentum flux observed in the ATOMIC region is likely applicable to other areas; i.e., wave-current interactions may be globally significant in modulating small-scale variability in waves and air-sea fluxes even outside of locations with large wind or current variations. This finding is of particular relevance to model simulations that do not account for small-scale spatial variations in surface currents, or those that do not incorporate wave-current interactions at all or comprehensively into air-sea flux parameterizations. Due to greater small-scale spatial variability in coastal areas, the influence of wave-current interactions on air-sea fluxes is likely significantly greater here, along with locations that have stronger mesoscale and submesoscale eddy activity such as near strong western boundary currents like the North Brazil Current region to the south of the ATOMIC study area (Figure 2).

5 Conclusions

Typically, in the northwest tropical Atlantic trade wind region during winter, currents follow the waves at 0 to 0.3 ms^{-1}. Currents also occasionally (11% of observations) follow the waves by greater than 0.3 ms^{-1}. Conditions where currents were in the opposite direction as the waves occurred approximately 11% of the time, preferentially when wind speeds were below 8 ms^{-1}. Opposing wave-relative currents were never greater than 0.16 ms^{-1}. The three case studies demonstrate that surface current speed and directional variability exists on a wide range of spatial scales, from a few kilometers (Figure 5) to the scales of mesoscale features (Figure 7), and produces variations in mss and u_* on the same scales.

In conditions where the currents follow the waves (green and blue lines in Figure 9), mss and u_* deviate by up to 20% from conditions where the currents are neutral or wave-opposing (pink and orange lines in Figure 9) in moderate wind conditions. Significant variations in mss and u_* also are present across different levels of wave-following current conditions. Variability in mss and u_* is greater than expected from the current-relative wind speed alone (Figure 1a), which implies that variability in u_* at constant wind speeds is the result of a combination of the current-relative wind and Doppler shift effects of waves. The Doppler shift changes the waves' slopes, and these changes in roughness are used to infer changes in momentum flux.

These findings suggest that wave-current interactions are a source of uncertainty in predictions of mss or u_* from either wind speed or current-relative wind speed alone,

and predictions of wind speed from u_* such as those by Voermans et al. (2020). Variations in u_* of 20% roughly equate to variations in momentum flux of 40% at a given wind speed (Equation 1). This significant contribution suggests that the inclusion of wave-current interactions in models and parameterizations is crucial for obtaining accurate estimates of waves and air-sea heat, gas, and momentum fluxes. Existing parameterizations of waves and surface currents, such as those from version 3.6 of the COARE bulk flux algorithm, do not comprehensively consider the effect of wave-current interactions. Hence, even though the mean flux is still well represented by these models, they underestimate the range variability of air-sea fluxes in the presences of varying surface currents and waves (Figure 10).

Data Availability Statement

SWIFT data are available through NOAA National Centers for Environmental Information (NCEI) at `https://doi.org/10.25921/s5d7-tc07` (Thomson et al., 2021). Meteorological observations from the NOAA Ship Ronald H. Brown are also available through NOAA NCEI at `https://doi.org/10.25921/etxb-ht19`. Coastline data in Figure 2 were obtained using the NOAA Global Self-consistent Hierarchical High-resolution Geography Database (GSHHG). Reprocessed satellite sea level anomalies used to calculate eddy kinetic energy are available through CMEMS at `https://resources.marine.copernicus.eu/?option=com_csw&view=details&product_id=SEALEVEL_GLO_PHY_L4_REP_OBSERVATIONS_008_047`. Version 3.6 of the COARE bulk flux algorithm is available at `ftp://ftp1.esrl.noaa.gov/BLO/Air-Sea/bulkalg/cor3_6/`.

Acknowledgments

We thank Kristin Zeiden (APL-UW) for reviewing a version of the manuscript and providing many valuable suggestions. We thank Alex de Klerk (APL-UW) for engineering the SWIFT drifters and for extensive assistance in deploying and recovering the vehicles. We thank Joe Talbert (APL-UW) for engineering the SWIFTs. We appreciate conversations with Chris Fairall (NOAA PSL) regarding the COARE algorithm. We acknowledge the scientists, captain, and crew on the two cruise legs of the 2020 ATOMIC field campaign on the NOAA Ship Ronald H. Brown for their assistance in collecting much of the observational data used in this study. Perceptually uniform colormaps used in Figure 2 were obtained from the cmocean package (Thyng et al., 2016). This work was supported by NOAA CPO CVP Award NA19OAR4310374.

References

Agrawal, Y. C., Terray, E. A., Donelan, M. A., Hwang, P. A., Williams III, A. J., Drennan, W. M., ... Kitaigorodskii, S. A. (1992). Enhanced dissipation of kinetic energy beneath surface waves. *Nature*, *359*(6392), 219. (https://doi.org/10.1038/359219a0)

Akan, Ç., McWilliams, J. C., Moghimi, S., & Özkan-Haller, H. T. (2018). Frontal dynamics at the edge of the Columbia River plume. *Ocean Modelling*, *122*, 1–12. (https://doi.org/10.1016/j.ocemod.2017.12.001)

Akan, Ç., Moghimi, S., Özkan-Haller, H. T., Osborne, J., & Kurapov, A. (2017). On the dynamics of the mouth of the Columbia River: Results from a three-dimensional fully coupled wave-current interaction model. *Journal of Geophysical Research: Oceans*, *122*(7), 5218–5236. (https://doi.org/10.1002/2016JC012307)

Ardhuin, F., Chapron, B., & Elfouhaily, T. (2004). Waves and the air–sea momentum budget: Implications for ocean circulation modeling. *Journal of Physical Oceanography*, *34*(7), 1741–1755. (https://doi.org/10.1175/1520-

0485(2004)034¡1741:WATAMB¿2.0.CO;2)

Ardhuin, F., Gille, S. T., Menemenlis, D., Rocha, C. B., Rascle, N., Chapron, B., ... Molemaker, J. (2017). Small-scale open ocean currents have large effects on wind wave heights. *Journal of Geophysical Research: Oceans*, *122*(6), 4500–4517. (https://doi.org/10.1002/2016JC012413)

Banihashemi, S., & Kirby, J. T. (2019). Approximation of wave action conservation in vertically sheared mean flows. *Ocean Modelling*, *143*, 101460. (https://doi.org/10.1016/j.ocemod.2019.101460)

Banihashemi, S., Kirby, J. T., & Dong, Z. (2017). Approximation of wave action flux velocity in strongly sheared mean flows. *Ocean Modelling*, *116*, 33–47. (https://doi.org/10.1016/j.ocemod.2017.06.002)

Banner, M. L. (1990). Equilibrium spectra of wind waves. *Journal of Physical Oceanography*, *20*(7), 966–984. (https://doi.org/10.1175/1520-0485(1990)020¡0966:ESOWW¿2.0.CO;2)

Banner, M. L., Gemmrich, J. R., & Farmer, D. M. (2002). Multiscale measurements of ocean wave breaking probability. *Journal of physical oceanography*, *32*(12), 3364–3375. (https://doi.org/10.1175/1520-0485(2002)032¡3364:MMOOWB¿2.0.CO;2)

Banner, M. L., & Morison, R. P. (2010). Refined source terms in wind wave models with explicit wave breaking prediction. Part I: Model framework and validation against field data. *Ocean Modelling*, *33*(1-2), 177–189. (https://doi.org/10.1016/j.ocemod.2010.01.002)

Branch, R. A., Horner-Devine, A. R., Akan, C., Chickadel, C. C., Farquharson, G., Hudson, A., ... Jessup, A. T. (2018). Airborne LiDAR measurements and model simulations of tides, waves, and surface slope at the mouth of the Columbia River. *IEEE Transactions on Geoscience and Remote Sensing*, *56*(12), 7038–7048. (https://doi.org/10.1109/TGRS.2018.2847561)

Businger, J., & Shaw, W. (1984). The response of the marine boundary layer to mesoscale variations in sea-surface temperature. *Dynamics of Atmospheres and Oceans*, *8*(3-4), 267–281. (https://doi.org/10.1016/0377-0265(84)90012-5)

Campana, J., Terrill, E. J., & De Paolo, T. (2016). The development of an inversion technique to extract vertical current profiles from X-band radar observations. *Journal of Atmospheric and Oceanic Technology*, *33*(9), 2015–2028. (https://doi.org/10.1175/JTECH-D-15-0145.1)

Chawla, A., & Kirby, J. T. (2002). Monochromatic and random wave breaking at blocking points. *Journal of Geophysical Research: Oceans*, *107*(C7), 4–1. (https://doi.org/10.1029/2001JC001042)

Chelton, D. B., Esbensen, S. K., Schlax, M. G., Thum, N., Freilich, M. H., Wentz, F. J., ... Schopf, P. S. (2001). Observations of coupling between surface wind stress and sea surface temperature in the eastern tropical Pacific. *Journal of Climate*, *14*(7), 1479–1498. (https://doi.org/10.1175/1520-0442(2001)014¡1479:OOCBSW¿2.0.CO;2)

Chelton, D. B., Schlax, M. G., Freilich, M. H., & Milliff, R. F. (2004). Satellite measurements reveal persistent small-scale features in ocean winds. *Science*, *303*(5660), 978–983. (https://doi.org/10.1126/science.1091901)

Chen, H., & Zou, Q. (2018). Characteristics of wave breaking and blocking by spatially varying opposing currents. *Journal of Geophysical Research: Oceans*, *123*(5), 3761–3785. (https://doi.org/10.1029/2017JC013440)

Choi, W. (2009). Nonlinear surface waves interacting with a linear shear current. *Mathematics and Computers in Simulation*, *80*(1), 29–36. (https://doi.org/10.1016/j.matcom.2009.06.021)

Coles, V. J., Brooks, M. T., Hopkins, J., Stukel, M. R., Yager, P. L., & Hood, R. R. (2013). The pathways and properties of the Amazon River Plume in the tropical North Atlantic Ocean. *Journal of Geophysical Research: Oceans*, *118*(12), 6894–6913. (https://doi.org/10.1002/2013JC008981)

Collins, C., Potter, H., Lund, B., Tamura, H., & Graber, H. C. (2018). Directional wave spectra observed during intense tropical cyclones. *Journal of Geophysical Research: Oceans*, *123*(2), 773–793. (https://doi.org/10.1002/2017JC012943)

Craig, P. D., & Banner, M. L. (1994). Modeling wave-enhanced turbulence in the ocean surface layer. *Journal of Physical Oceanography*, *24*(12), 2546–2559. (https://doi.org/10.1175/1520-0485(1994)024¡2546:MWETIT¿2.0.CO;2)

Derakhti, M., Thomson, J., & Kirby, J. T. (2020). Sparse sampling of intermittent turbulence generated by breaking surface waves. *Journal of Physical Oceanography*, *50*(4), 867–885. (https://doi.org/10.1175/JPO-D-19-0138.1)

Ebuchi, N., & Hanawa, K. (2000). Mesoscale eddies observed by TOLEX-ADCP and TOPEX/POSEIDON altimeter in the Kuroshio recirculation region south of Japan. *Journal of Oceanography*, *56*(1), 43–57. (https://doi.org/10.1023/A:1011110507628)

Edson, J. B., Jampana, V., Weller, R. A., Bigorre, S. P., Plueddemann, A. J., Fairall, C. W., ... Hersbach, H. (2013). On the exchange of momentum over the open ocean. *Journal of Physical Oceanography*, *43*(8), 1589–1610. (https://doi.org/10.1175/JPO-D-12-0173.1)

Ellingsen, S. Å., & Li, Y. (2017). Approximate dispersion relations for waves on arbitrary shear flows. *Journal of Geophysical Research: Oceans*, *122*(12), 9889–9905. (https://doi.org/10.1002/2017JC012994)

Fairall, C. W., Bradley, E. F., Hare, J., Grachev, A. A., & Edson, J. B. (2003). Bulk parameterization of air–sea fluxes: Updates and verification for the COARE algorithm. *Journal of Climate*, *16*(4), 571–591. (https://doi.org/10.1175/1520-0442(2003)016¡0571:BPOASF¿2.0.CO;2)

Fairall, C. W., Bradley, E. F., Rogers, D. P., Edson, J. B., & Young, G. S. (1996). Bulk parameterization of air-sea fluxes for Tropical Ocean-Global Atmosphere Coupled-Ocean Atmosphere Response Experiment. *Journal of Geophysical Research: Oceans*, *101*(C2), 3747–3764. (https://doi.org/10.1029/95JC03205)

Ffield, A. (2005). North Brazil current rings viewed by TRMM Microwave Imager SST and the influence of the Amazon Plume. *Deep Sea Research Part I: Oceanographic Research Papers*, *52*(1), 137–160. (https://doi.org/10.1016/j.dsr.2004.05.013)

Fisher, A. W., Sanford, L. P., Scully, M. E., & Suttles, S. E. (2017). Surface wave effects on the translation of wind stress across the air–sea interface in a fetch-limited, coastal embayment. *Journal of Physical Oceanography*, *47*(8), 1921–1939. (https://doi.org/10.1175/JPO-D-16-0146.1)

Fratantoni, D. M., & Glickson, D. A. (2002). North Brazil Current ring generation and evolution observed with SeaWiFS. *Journal of Physical Oceanography*, *32*(3), 1058–1074. (https://doi.org/10.1175/1520-0485(2002)032¡1058:NBCRGA¿2.0.CO;2)

Fratantoni, D. M., & Richardson, P. L. (2006). The evolution and demise of North Brazil Current rings. *Journal of Physical Oceanography*, *36*(7), 1241–1264. (https://doi.org/10.1175/JPO2907.1)

Friehe, C., Shaw, W., Rogers, D., Davidson, K., Large, W., Stage, S., ... Li, F. (1991). Air-sea fluxes and surface layer turbulence around a sea surface temperature front. *Journal of Geophysical Research: Oceans*, *96*(C5), 8593–8609. (https://doi.org/10.1029/90JC02062)

Gaube, P., Chelton, D. B., Samelson, R. M., Schlax, M. G., & ONeill, L. W. (2015). Satellite observations of mesoscale eddy-induced Ekman pumping. *Journal of Physical Oceanography*, *45*(1), 104–132. (https://doi.org/10.1175/JPO-D-14-0032.1)

Gemmrich, J., & Pawlowicz, R. (2020). Wind Waves in the Strait of Georgia. *Atmosphere-Ocean*, *58*(2), 79–97. (https://doi.org/10.1080/07055900.2020.1735989)

Haus, B. K. (2007). Surface current effects on the fetch-limited growth

of wave energy. *Journal of Geophysical Research: Oceans*, *112*(C3). (https://doi.org/10.1029/2006JC003924)

Hegermiller, C. A., Warner, J. C., Olabarrieta, M., & Sherwood, C. R. (2019). Wave–Current Interaction between Hurricane Matthew Wave Fields and the Gulf Stream. *Journal of Physical Oceanography*, *49*(11), 2883–2900. (https://doi.org/10.1175/JPO-D-19-0124.1)

Holthuijsen, L., & Tolman, H. (1991). Effects of the Gulf Stream on ocean waves. *Journal of Geophysical Research: Oceans*, *96*(C7), 12755–12771. (https://doi.org/10.1029/91JC00901)

Janssen, P. A. (1989). Wave-induced stress and the drag of air flow over sea waves. *Journal of Physical Oceanography*, *19*(6), 745–754. (https://doi.org/10.1175/1520-0485(1989)019¡0745:WISATD¿2.0.CO;2)

Juszko, B.-A., Marsden, R. F., & Waddell, S. R. (1995). Wind stress from wave slopes using Phillips equilibrium theory. *Journal of Physical Oceanography*, *25*(2), 185–203. (https://doi.org/10.1175/1520-0485(1995)025¡0185:WSFWSU¿2.0.CO;2)

Kastner, S. E., Horner-Devine, A. R., & Thomson, J. (2018). The influence of wind and waves on spreading and mixing in the Fraser River plume. *Journal of Geophysical Research: Oceans*, *123*(9), 6818–6840. (https://doi.org/10.1029/2018JC013765)

Kim, S. Y. (2010). Observations of submesoscale eddies using high-frequency radar-derived kinematic and dynamic quantities. *Continental Shelf Research*, *30*(15), 1639–1655. (https://doi.org/10.1016/j.csr.2010.06.011)

Kitaigorodskii, S. (1983). On the theory of the equilibrium range in the spectrum of wind-generated gravity waves. *Journal of Physical Oceanography*, *13*(5), 816–827. (https://doi.org/10.1175/1520-0485(1983)013¡0816:OTTOTE¿2.0.CO;2)

Kudryavtsev, V., Yurovskaya, M., Chapron, B., Collard, F., & Donlon, C. (2017). Sun glitter imagery of surface waves. part 2: Waves transformation on ocean currents. *Journal of Geophysical Research: Oceans*, *122*(2), 1384–1399. (https://doi.org/10.1002/2016JC012426)

Large, W., & Pond, S. (1981). Open ocean momentum flux measurements in moderate to strong winds. *Journal of Physical Oceanography*, *11*(3), 324–336. (https://doi.org/10.1175/1520-0485(1981)011¡0324:OOMFMI¿2.0.CO;2)

Lenain, L., & Melville, W. K. (2017). Measurements of the directional spectrum across the equilibrium saturation ranges of wind-generated surface waves. *Journal of Physical Oceanography*, *47*(8), 2123–2138. (https://doi.org/10.1175/JPO-D-17-0017.1)

Lindzen, R. S., & Nigam, S. (1987). On the role of sea surface temperature gradients in forcing low-level winds and convergence in the tropics. *Journal of Atmospheric Sciences*, *44*(17), 2418–2436. (https://doi.org/10.1175/1520-0469(1987)044¡2418:OTROSS¿2.0.CO;2)

Lygre, A., & Krogstad, H. E. (1986). Maximum entropy estimation of the directional distribution in ocean wave spectra. *Journal of Physical Oceanography*, *16*(12), 2052–2060. (https://doi.org/10.1175/1520-0485(1986)016¡2052:MEEOTD¿2.0.CO;2)

McWilliams, J. C. (2016). Submesoscale currents in the ocean. *Proceedings of the Royal Society A: Mathematical, Physical and Engineering Sciences*, *472*(2189), 20160117. (https://doi.org/10.1098/rspa.2016.0117)

McWilliams, J. C. (2018). Surface wave effects on submesoscale fronts and filaments. *Journal of Fluid Mechanics*, *843*, 479. (https://doi.org/10.1017/jfm.2018.158)

Moghimi, S., Özkan-Haller, H. T., Akan, Ç., & Jurisa, J. T. (2019). Mechanistic analysis of the wave-current interaction in the plume region of a partially mixed tidal inlet. *Ocean Modelling*, *134*, 110–126. (https://doi.org/10.1016/j.ocemod.2018.12.003)

Molinari, R. L., Spillane, M., Brooks, I., Atwood, D., & Duckett, C. (1981).

Surface currents in the Caribbean Sea as deduced from Lagrangian observations. *Journal of Geophysical Research: Oceans*, *86*(C7), 6537–6542. (https://doi.org/10.1029/JC086iC07p06537)

Phillips, O. (1984). On the response of short ocean wave components at a fixed wavenumber to ocean current variations. *Journal of Physical Oceanography*, *14*(9), 1425–1433. (https://doi.org/10.1175/1520-0485(1984)014¡1425:OTROSO¿2.0.CO;2)

Phillips, O. (1985). Spectral and statistical properties of the equilibrium range in wind-generated gravity waves. *Journal of Fluid Mechanics*, *156*, 505–531. (https://doi.org/10.1017/S0022112085002221)

Pincus, R., Fairall, C. W., Bailey, A., Chen, H., Chuang, P. Y., de Boer, G., ... others (2021). Observations from the NOAA P-3 aircraft during ATOMIC. *Earth System Science Data*, *13*(7), 3281–3296. (https://doi.org/10.5194/essd-2021-11)

Plant, W. J. (1982). A relationship between wind stress and wave slope. *Journal of Geophysical Research: Oceans*, *87*(C3), 1961–1967. (https://doi.org/10.1029/JC087iC03p01961)

Quilfen, Y., & Chapron, B. (2019). Ocean surface wave-current signatures from satellite altimeter measurements. *Geophysical Research Letters*, *46*(1), 253–261. (https://doi.org/10.1029/2018GL081029)

Quilfen, Y., Yurovskaya, M., Chapron, B., & Ardhuin, F. (2018). Storm waves focusing and steepening in the Agulhas current: Satellite observations and modeling. *Remote Sensing of Environment*, *216*, 561–571. (https://doi.org/10.1016/j.rse.2018.07.020)

Quinn, P. K., Thompson, E. J., Coffman, D. J., Baidar, S., Bariteau, L., Bates, T. S., ... others (2021). Measurements from the RV Ronald H. Brown and related platforms as part of the Atlantic Tradewind Ocean-Atmosphere Mesoscale Interaction Campaign (ATOMIC). *Earth System Science Data*, *13*(4), 1759–1790. (https://doi.org/10.5194/essd-13-1759-2021)

Rapizo, H., Durrant, T. H., & Babanin, A. V. (2018). An assessment of the impact of surface currents on wave modeling in the Southern Ocean. *Ocean Dynamics*, *68*(8), 939–955. (https://doi.org/10.1007/s10236-018-1171-7)

Rascle, N., Chapron, B., Ponte, A., Ardhuin, F., & Klein, P. (2014). Surface roughness imaging of currents shows divergence and strain in the wind direction. *Journal of Physical Oceanography*, *44*(8), 2153–2163. (https://doi.org/10.1175/JPO-D-13-0278.1)

Rascle, N., Molemaker, J., Marié, L., Nouguier, F., Chapron, B., Lund, B., & Mouche, A. (2017). Intense deformation field at oceanic front inferred from directional sea surface roughness observations. *Geophysical Research Letters*, *44*(11), 5599–5608. (https://doi.org/10.1002/2017GL073473)

Redelsperger, J.-L., Bouin, M.-N., Pianezze, J., Garnier, V., & Marié, L. (2019). Impact of a sharp, small-scale SST front on the marine atmospheric boundary layer on the Iroise Sea: Analysis from a hectometric simulation. *Quarterly Journal of the Royal Meteorological Society*, *145*(725), 3692–3714. (https://doi.org/10.1002/qj.3650)

Reverdin, G., Olivier, L., Foltz, G., Speich, S., Karstensen, J., Horstmann, J., ... others (2021). Formation and evolution of a freshwater plume in the northwestern tropical Atlantic in February 2020. *Journal of Geophysical Research: Oceans*, *126*(4), e2020JC016981. (https://doi.org/10.1029/2020JC016981)

Romero, L., Hypolite, D., & McWilliams, J. C. (2020). Submesoscale current effects on surface waves. *Ocean Modelling*, *153*, 101662. (https://doi.org/10.1016/j.ocemod.2020.101662)

Romero, L., Hypolite, D., & McWilliams, J. C. (2021). Representing wave effects on currents. *Ocean Modelling*, 101873. (https://doi.org/10.1016/j.ocemod.2021.101873)

Romero, L., Lenain, L., & Melville, W. K. (2017). Observations of surface wave–current interaction. *Journal of Physical Oceanography*, *47*(3), 615–632. (https://doi.org/10.1175/JPO-D-16-0108.1)

Schwendeman, M., & Thomson, J. (2015). Observations of whitecap coverage and the relation to wind stress, wave slope, and turbulent dissipation. *Journal of Geophysical Research: Oceans*, *120*(12), 8346–8363. (https://doi.org/10.1002/2015JC011196)

Shao, M., Ortiz-Suslow, D. G., Haus, B. K., Lund, B., Williams, N. J., Özgökmen, T. M., ... Klymak, J. M. (2019). The variability of winds and fluxes observed near submesoscale fronts. *Journal of Geophysical Research: Oceans*, *124*(11), 7756–7780. (https://doi.org/10.1029/2019JC015236)

Smit, P. B., & Janssen, T. T. (2019). Swell propagation through submesoscale turbulence. *Journal of Physical Oceanography*, *49*(10), 2615–2630. (https://doi.org/10.1175/JPO-D-18-0250.1)

Smith, S. D. (1980). Wind stress and heat flux over the ocean in gale force winds. *Journal of Physical Oceanography*, *10*(5), 709–726. (https://doi.org/10.1175/1520-0485(1980)010¡0709:WSAHFO¿2.0.CO;2)

Stevens, B., Bony, S., Farrell, D., Ament, F., Blyth, A., Fairall, C., ... others (2021). EUREC^{4}A. *Earth System Science Data Discussions*, 1–78. (https://doi.org/10.5194/essd-2021-18)

Suzuki, N., Fox-Kemper, B., Hamlington, P. E., & Van Roekel, L. P. (2016). Surface waves affect frontogenesis. *Journal of Geophysical Research: Oceans*, *121*(5), 3597–3624. (https://doi.org/10.1002/2015JC011563)

Tang, C., Perrie, W., Jenkins, A., DeTracey, B., Hu, Y., Toulany, B., & Smith, P. (2007). Observation and modeling of surface currents on the Grand Banks: A study of the wave effects on surface currents. *Journal of Geophysical Research: Oceans*, *112*(C10). (https://doi.org/10.1029/2006JC004028)

Terray, E. A., Donelan, M., Agrawal, Y., Drennan, W. M., Kahma, K., Williams, A. J., ... Kitaigorodskii, S. (1996). Estimates of kinetic energy dissipation under breaking waves. *Journal of Physical Oceanography*, *26*(5), 792–807. (https://doi.org/10.1175/1520-0485(1996)026¡0792:EOKEDU¿2.0.CO;2)

Thompson, E., Fairall, C., Pezoa, S., & Bariteau, L. (2021). *ATOMIC ship navigation, meteorology, seawater, fluxes: Near-surface meteorology, air-sea fluxes, surface ocean waves, and near surface ocean parameters (temperature, salinity, currents) and primary dataset of ship location and navigation estimated from in-situ and remote sensing instruments aboard NOAA Ship Ronald H. Brown in the North Atlantic Ocean, near Barbados: Atlantic Tradewind Ocean-Atmosphere Mesoscale Interaction Campaign 2020-01-09 to 2020-02-12 (NCEI Accession 0225427). NOAA National Centers for Environmental Information. Dataset. Accessed 17 June 2021.* doi: https://doi.org/10.25921/etxb-ht19

Thomson, J. (2012). Wave breaking dissipation observed with SWIFT drifters. *Journal of Atmospheric and Oceanic Technology*, *29*(12), 1866–1882. (https://doi.org/10.1175/JTECH-D-12-00018.1)

Thomson, J., D'Asaro, E., Cronin, M., Rogers, W., Harcourt, R., & Shcherbina, A. (2013). Waves and the equilibrium range at ocean weather station p. *Journal of Geophysical Research: Oceans*, *118*(11), 5951–5962. (https://doi.org/10.1002/2013JC008837)

Thomson, J., Girton, J. B., Jha, R., & Trapani, A. (2018). Measurements of directional wave spectra and wind stress from a wave glider autonomous surface vehicle. *Journal of Atmospheric and Oceanic Technology*, *35*(2), 347–363. (https://doi.org/10.1175/JTECH-D-17-0091.1)

Thomson, J., Horner-Devine, A. R., Zippel, S., Rusch, C., & Geyer, W. (2014). Wave breaking turbulence at the offshore front of the Columbia River plume. *Geophysical Research Letters*, *41*(24), 8987–8993. (https://doi.org/10.1002/2014GL062274)

Thomson, J., Moulton, M., de Klerk, A., Talbert, J., Guerra, M., Kastner, S., ... Nylund, S. (2019). A new version of the SWIFT platform for waves, currents, and turbulence in the ocean surface layer. In *2019 ieee/oes twelfth current, waves and turbulence measurement (cwtm)* (pp. 1–7). (https://doi.org/10.1109/CWTM43797.2019.8955299)

Thomson, J., Thompson, E., Iyer, S., Drushka, K., & de Klerk, A. (2021). *ATOMIC SWIFT drifters: Near-surface meteorology, air-sea fluxes, surface ocean waves, and near-surface ocean properties (turbulent dissipation rate, currents, temperature, salinity) estimated from in-situ and remote sensing instruments aboard six SWIFT drifters (Surface Wave Instrument Float with Tracking) launched and recovered for two different deployments from NOAA Ship Ronald H. Brown in the North Atlantic Ocean, near Barbados: Atlantic Tradewind Ocean-Atmosphere Mesoscale Interaction Campaign 2020-01-14 to 2020-02-11 (NCEI Accession 0225279). NOAA National Centers for Environmental Information. Dataset. Accessed 4 June 2021.* doi: https://doi.org/10.25921/s5d7-tc07

Thyng, K. M., Greene, C. A., Hetland, R. D., Zimmerle, H. M., & DiMarco, S. F. (2016). True colors of oceanography: Guidelines for effective and accurate colormap selection. *Oceanography*, *29*(3), 9–13. (https://doi.org/10.5670/oceanog.2016.66)

van Aken, H. M. (2002). Surface currents in the Bay of Biscay as observed with drifters between 1995 and 1999. *Deep Sea Research Part I: Oceanographic Research Papers*, *49*(6), 1071–1086. (https://doi.org/10.1016/S0967-0637(02)00017-1)

van der Westhuysen, A. J. (2012). Spectral modeling of wave dissipation on negative current gradients. *Coastal Engineering*, *68*, 17–30. (https://doi.org/10.1016/j.coastaleng.2012.05.001)

Vincent, C. L., Thomson, J., Graber, H. C., & Collins III, C. O. (2019). Impact of swell on the wind-sea and resulting modulation of stress. *Progress in Oceanography*, *178*, 102164. (https://doi.org/10.1016/j.pocean.2019.102164)

Voermans, J., Smit, P., Janssen, T., & Babanin, A. (2020). Estimating wind speed and direction using wave spectra. *Journal of Geophysical Research: Oceans*, *125*(2), e2019JC015717. (https://doi.org/10.1029/2019JC015717)

Wallace, J. M., Mitchell, T., & Deser, C. (1989). The influence of sea-surface temperature on surface wind in the eastern equatorial Pacific: Seasonal and interannual variability. *Journal of Climate*, *2*(12), 1492–1499. (https://doi.org/10.1175/1520-0442(1989)002¡1492:TIOSST¿2.0.CO;2)

Wang, P., & Sheng, J. (2016). A comparative study of wave-current interactions over the eastern Canadian shelf under severe weather conditions using a coupled wave-circulation model. *Journal of Geophysical Research: Oceans*, *121*(7), 5252–5281. (https://doi.org/10.1002/2016JC011758)

Wiles, P. J., Rippeth, T. P., Simpson, J. H., & Hendricks, P. J. (2006). A novel technique for measuring the rate of turbulent dissipation in the marine environment. *Geophysical Research Letters*, *33*(21). (https://doi.org/10.1029/2006GL027050)

Zippel, S., & Thomson, J. (2017). Surface wave breaking over sheared currents: Observations from the Mouth of the Columbia River. *Journal of Geophysical Research: Oceans*, *122*(4), 3311–3328. (https://doi.org/10.1002/2016JC012498)

Figure 1.

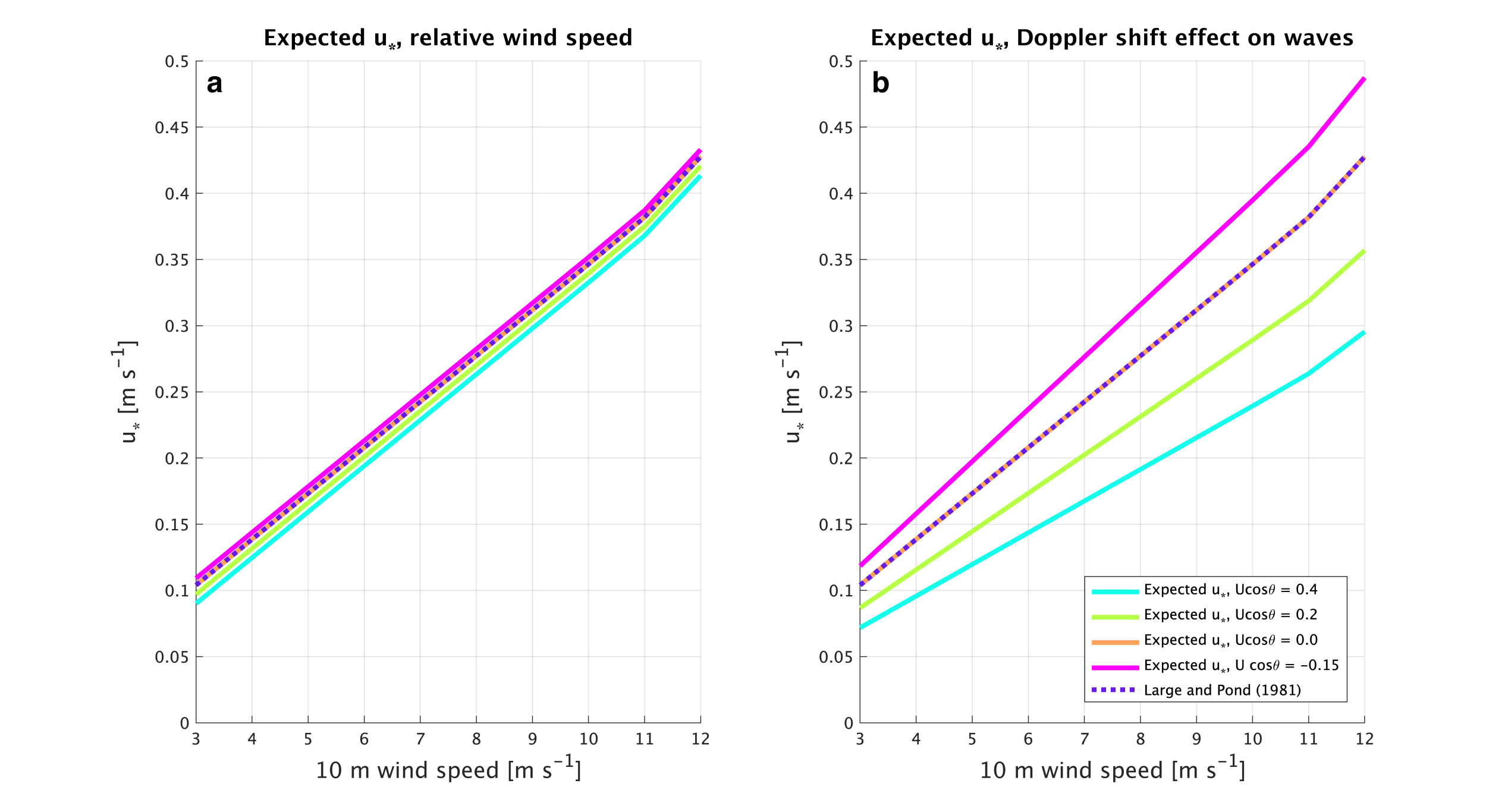
Expected u*, relative wind speed
a
u* [m s−1]
10 m wind speed [m s−1]
Expected u*, Doppler shift effect on waves
b
u* [m s−1]
10 m wind speed [m s−1]
Expected u*, Ucosθ = 0.4
Expected u*, Ucosθ = 0.2
Expected u*, Ucosθ = 0.0
Expected u*, U cosθ = −0.15
Large and Pond (1981)

Figure 2.

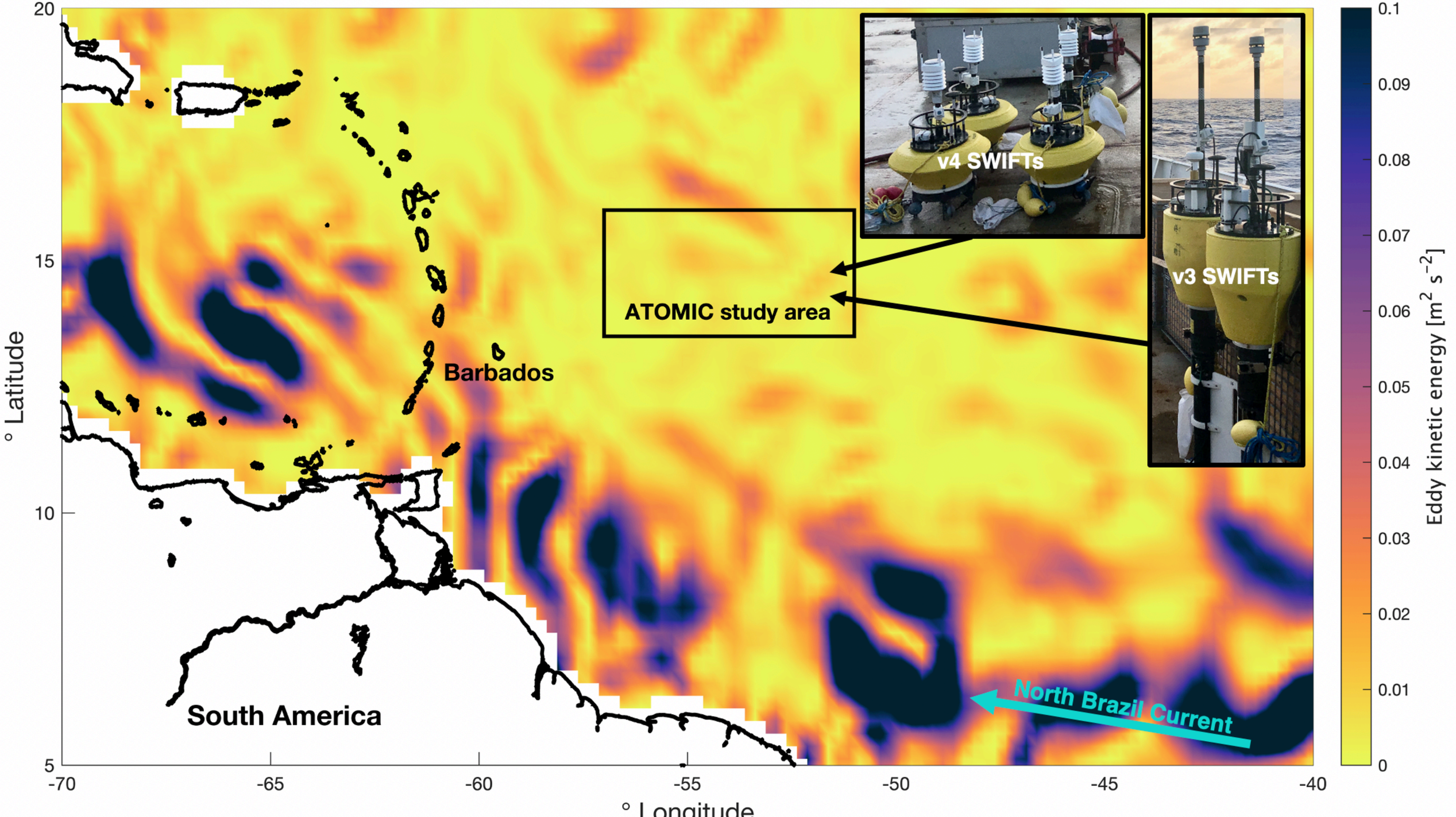
20
15
10
5
° Latitude
-70
-65
-60
-55
-50
-45
-40
° Longitude
Barbados
South America
ATOMIC study area
v4 SWIFTs
v3 SWIFTs
North Brazil Current
0.1
0.09
0.08
0.07
0.06
0.05
0.04
0.03
0.02
0.01
0
Eddy kinetic energy [m^2 s^{-2}]

Figure 3.

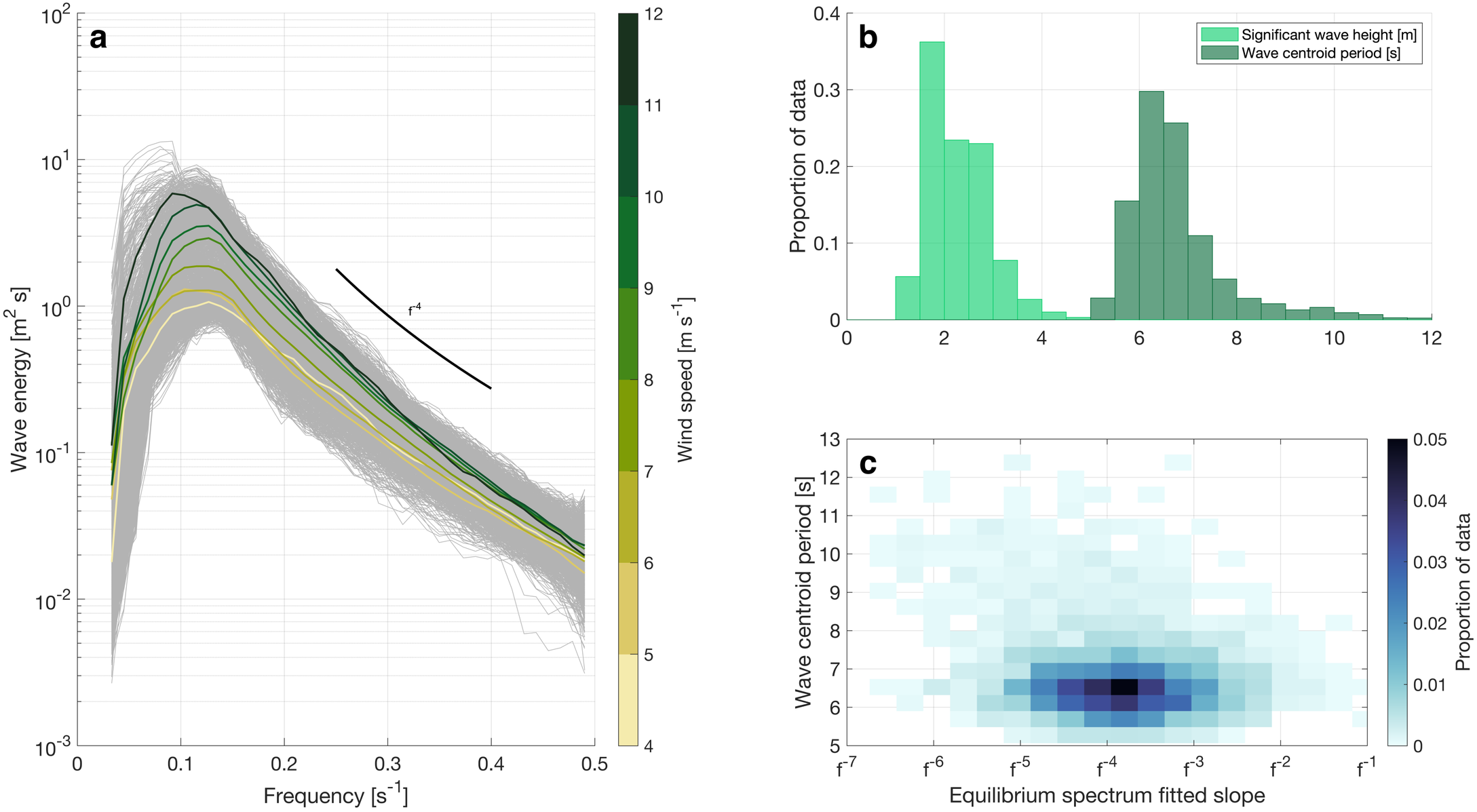
a
Wave energy [m^2 s]
Frequency [s^{-1}]
Wind speed [m s^{-1}]
f^{-4}
b
Significant wave height [m]
Wave centroid period [s]
Proportion of data
c
Wave centroid period [s]
Equilibrium spectrum fitted slope
Proportion of data

Figure 4.

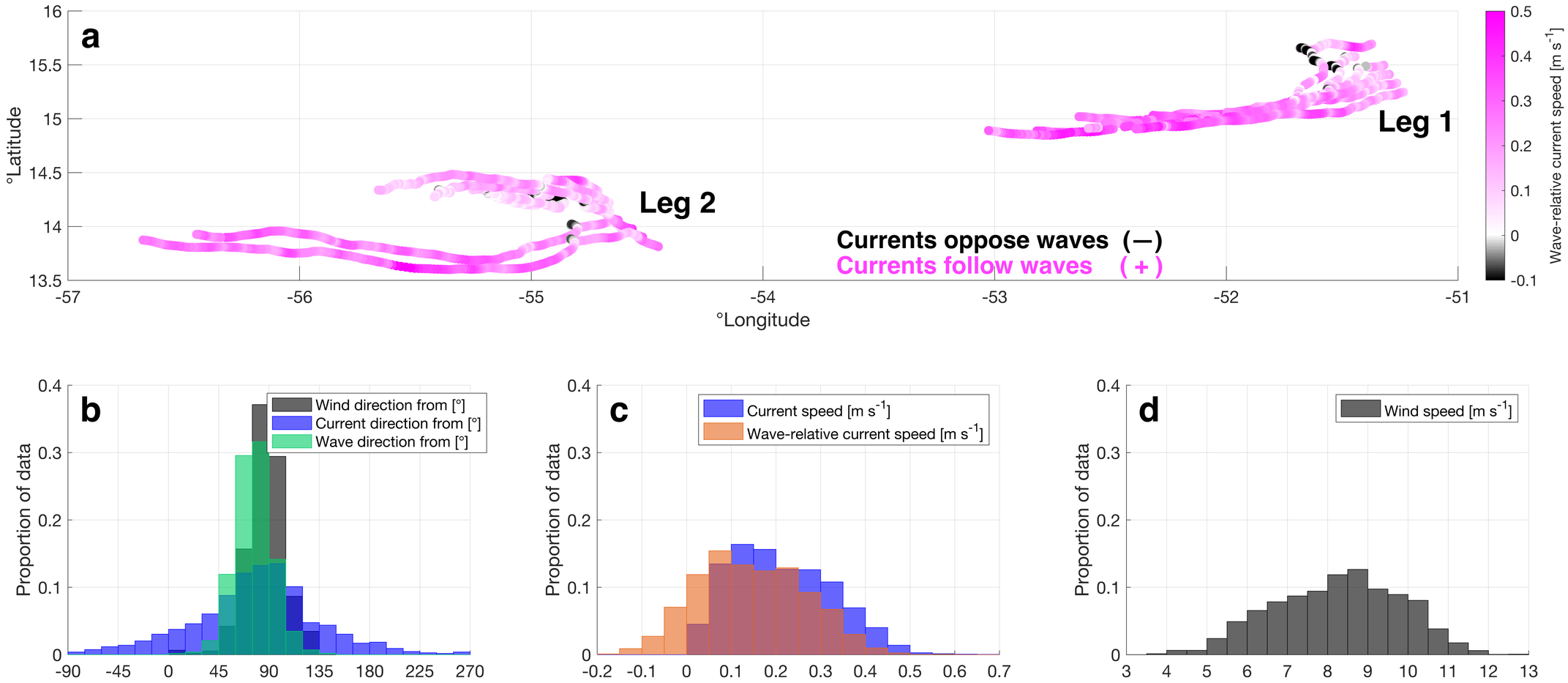
a
Leg 1
Leg 2
Currents oppose waves (−)
Currents follow waves (+)
°Latitude
°Longitude
Wave-relative current speed [m s-1]
b
Wind direction from [°]
Current direction from [°]
Wave direction from [°]
Proportion of data
c
Current speed [m s-1]
Wave-relative current speed [m s-1]
Proportion of data
d
Wind speed [m s-1]
Proportion of data

Figure 5.

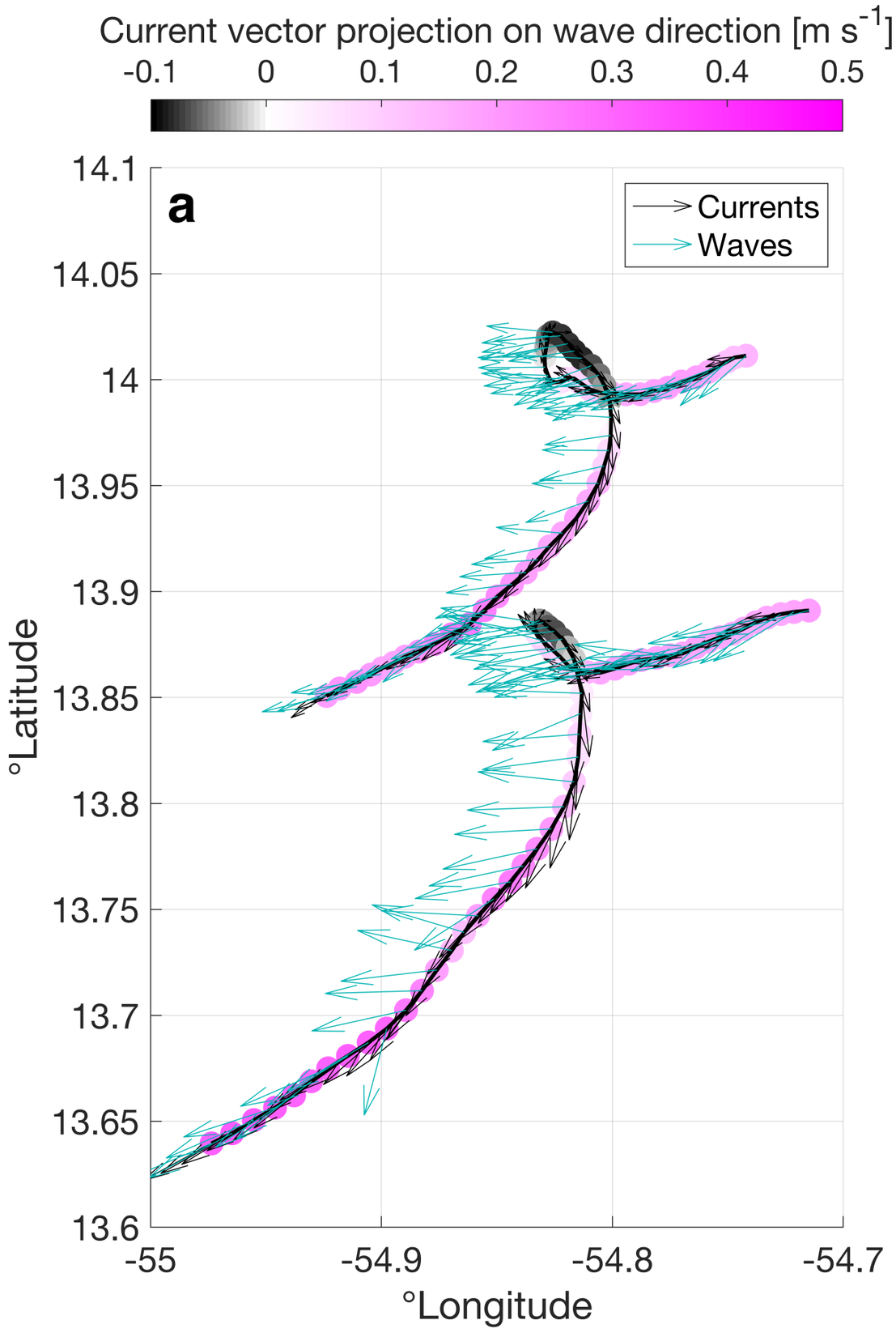
Current vector projection on wave direction [m s-1]
-0.1
0
0.1
0.2
0.3
0.4
0.5
a
Currents
Waves
14.1
14.05
14
13.95
13.9
13.85
13.8
13.75
13.7
13.65
13.6
°Latitude
-55
-54.9
-54.8
-54.7
°Longitude

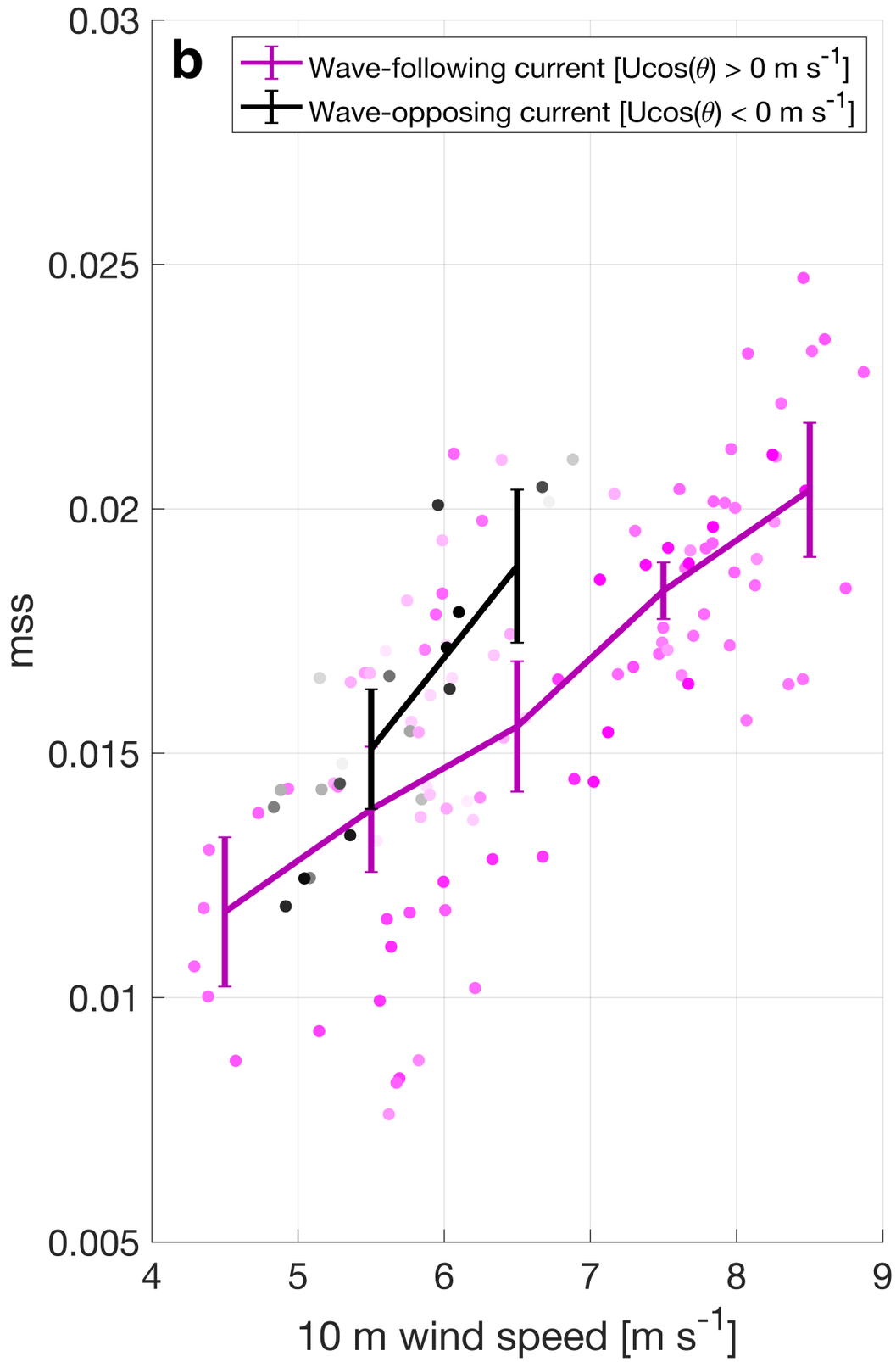
b
Wave-following current [Ucos(θ) > 0 m s-1]
Wave-opposing current [Ucos(θ) < 0 m s-1]
0.03
0.025
0.02
0.015
0.01
0.005
mss
4
5
6
7
8
9
10 m wind speed [m s-1]

Figure 6.

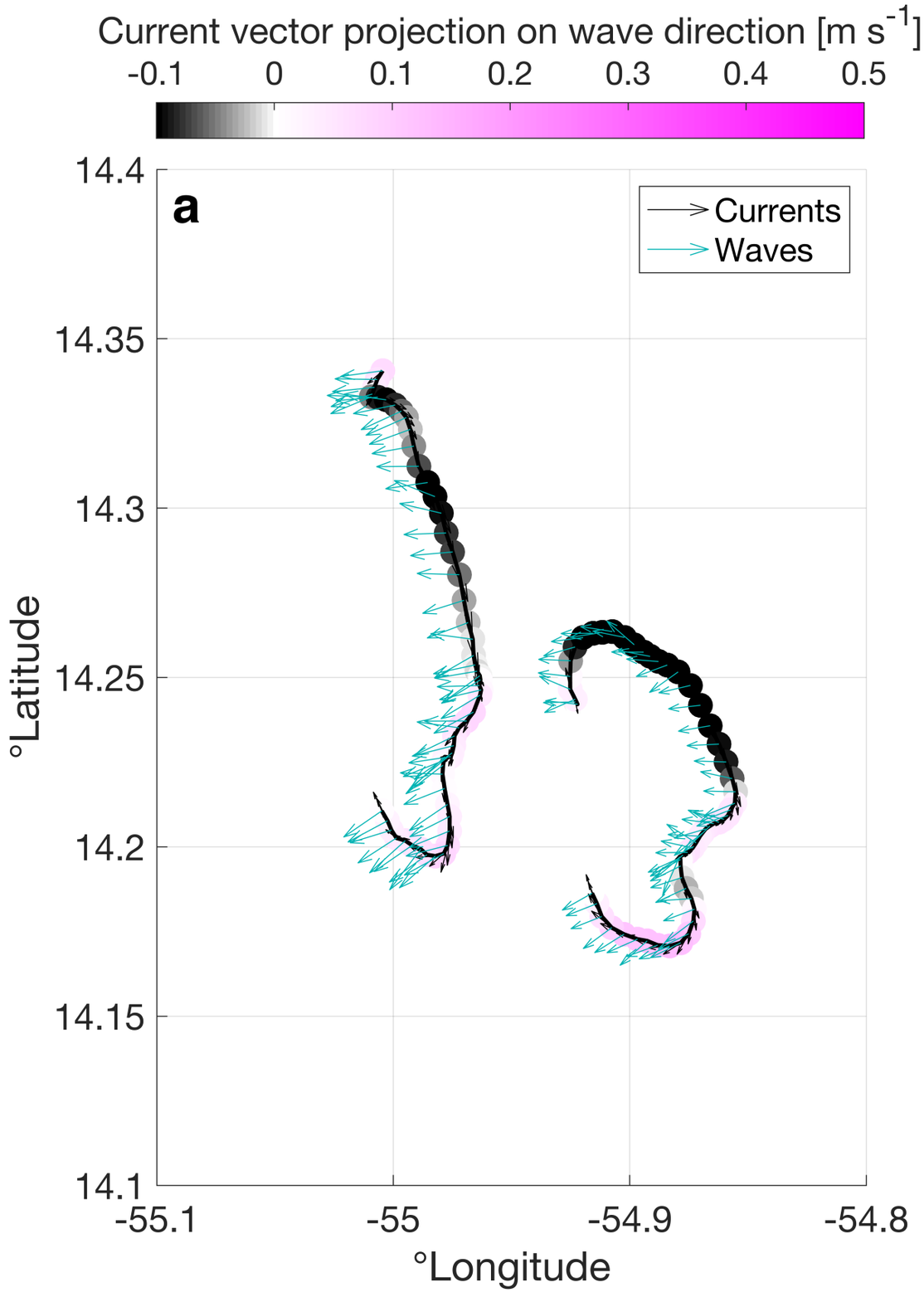
Current vector projection on wave direction [m s-1]
-0.1
0
0.1
0.2
0.3
0.4
0.5
a
Currents
Waves
14.4
14.35
14.3
14.25
14.2
14.15
14.1
°Latitude
-55.1
-55
-54.9
-54.8
°Longitude

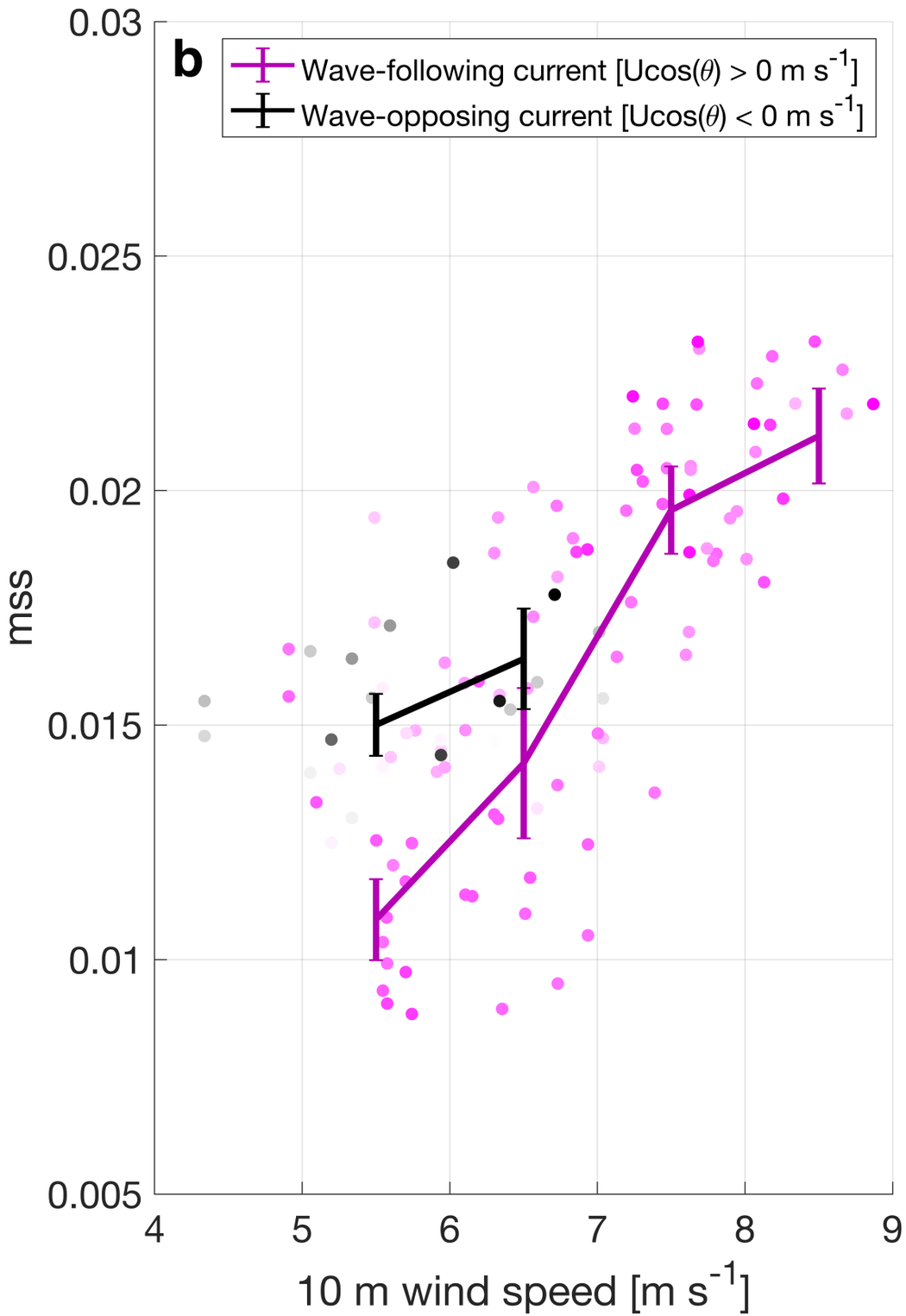
b
Wave-following current [Ucos(θ) > 0 m s-1]
Wave-opposing current [Ucos(θ) < 0 m s-1]
0.03
0.025
0.02
0.015
0.01
0.005
mss
4
5
6
7
8
9
10 m wind speed [m s-1]

Figure 7.

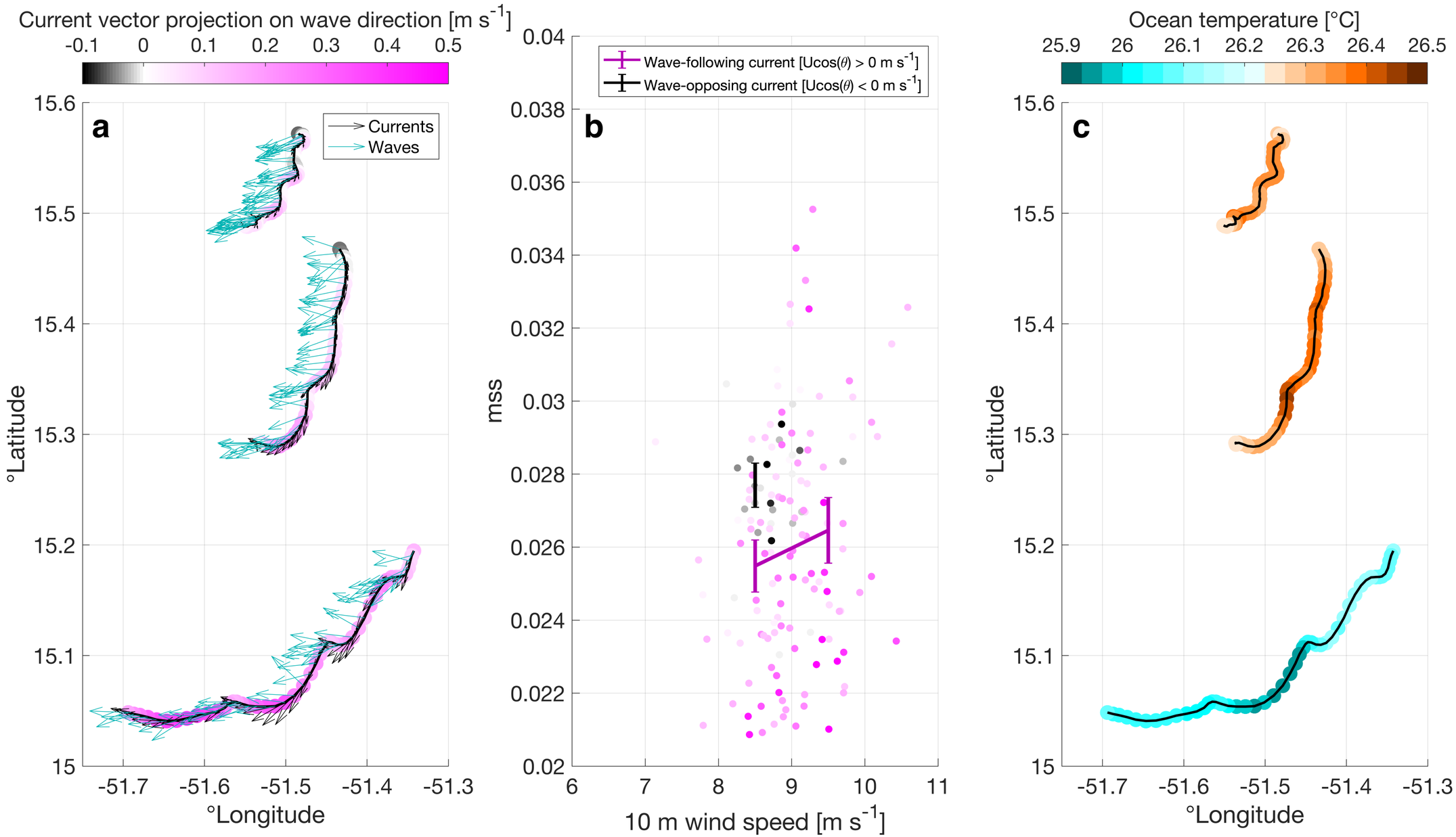
Current vector projection on wave direction [m s-1]
-0.1 0 0.1 0.2 0.3 0.4 0.5
a
Currents
Waves
°Latitude
°Longitude
15.6
15.5
15.4
15.3
15.2
15.1
15
-51.7 -51.6 -51.5 -51.4 -51.3
b
Wave-following current [Ucos(θ) > 0 m s-1]
Wave-opposing current [Ucos(θ) < 0 m s-1]
mss
10 m wind speed [m s-1]
0.04
0.038
0.036
0.034
0.032
0.03
0.028
0.026
0.024
0.022
0.02
6 7 8 9 10 11
Ocean temperature [°C]
25.9 26 26.1 26.2 26.3 26.4 26.5
c
°Latitude
°Longitude

Figure 8.

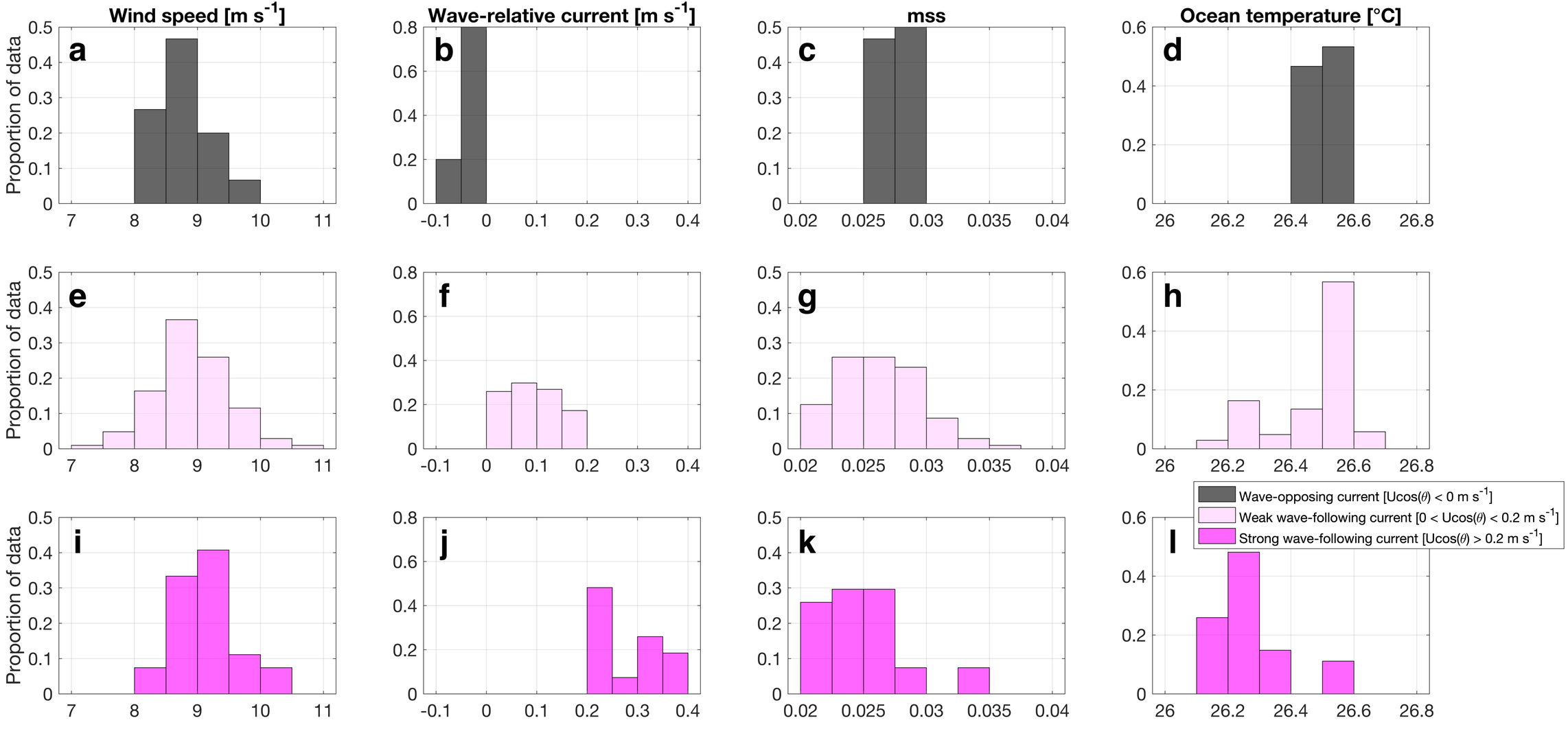
Wind speed [m s-1]
Wave-relative current [m s-1]
mss
Ocean temperature [°C]
Proportion of data
a
b
c
d
e
f
g
h
i
j
k
l
Wave-opposing current [Ucos(θ) < 0 m s-1]
Weak wave-following current [0 < Ucos(θ) < 0.2 m s-1]
Strong wave-following current [Ucos(θ) > 0.2 m s-1]

Figure 9.

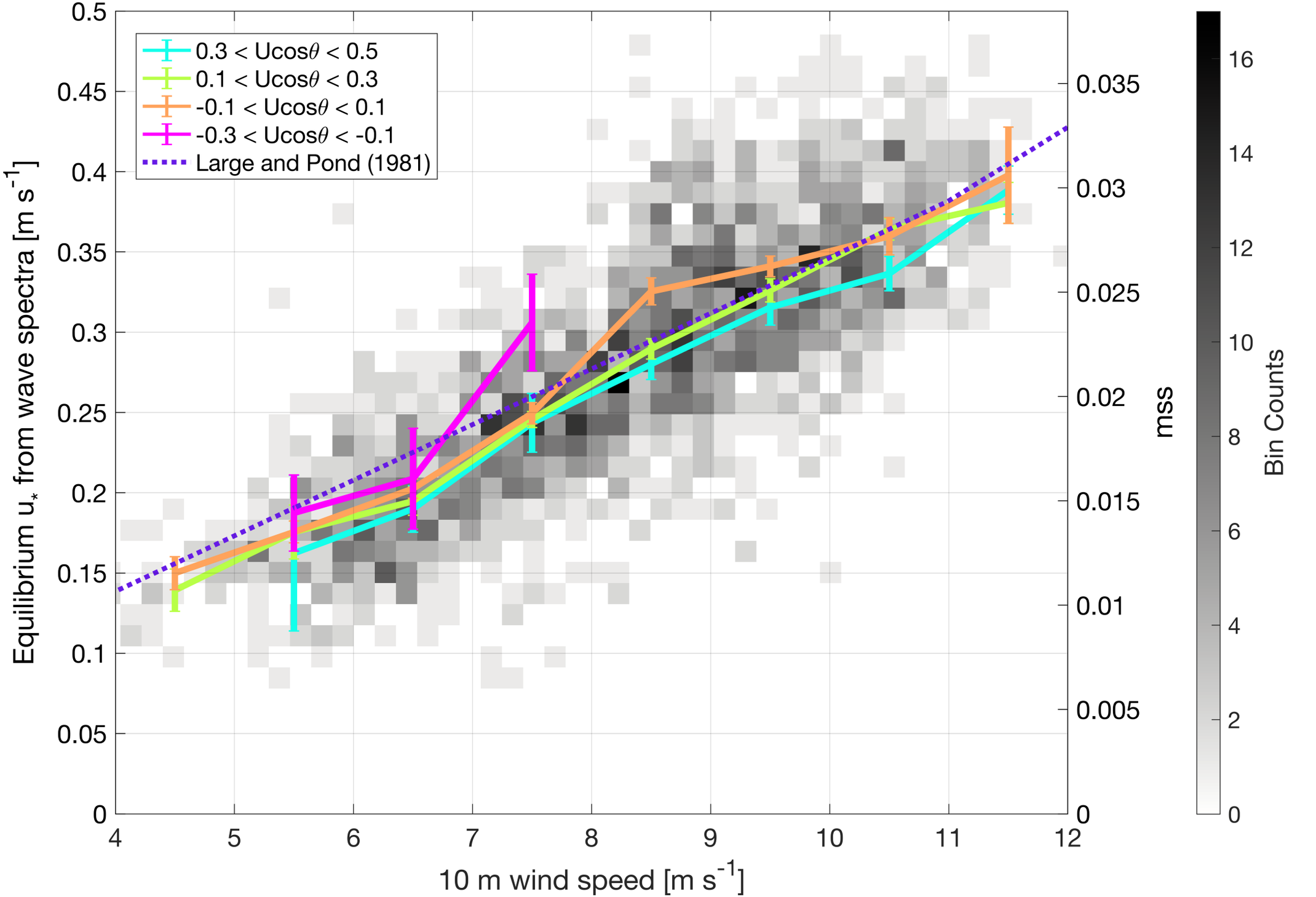
0.3 < Ucosθ < 0.5
0.1 < Ucosθ < 0.3
-0.1 < Ucosθ < 0.1
-0.3 < Ucosθ < -0.1
Large and Pond (1981)
Equilibrium u* from wave spectra [m s-1]
10 m wind speed [m s-1]
mss
Bin Counts
0
0.05
0.1
0.15
0.2
0.25
0.3
0.35
0.4
0.45
0.5
0.005
0.01
0.015
0.02
0.025
0.03
0.035
4
5
6
7
8
9
10
11
12
2
4
6
8
10
12
14
16

Figure 10.

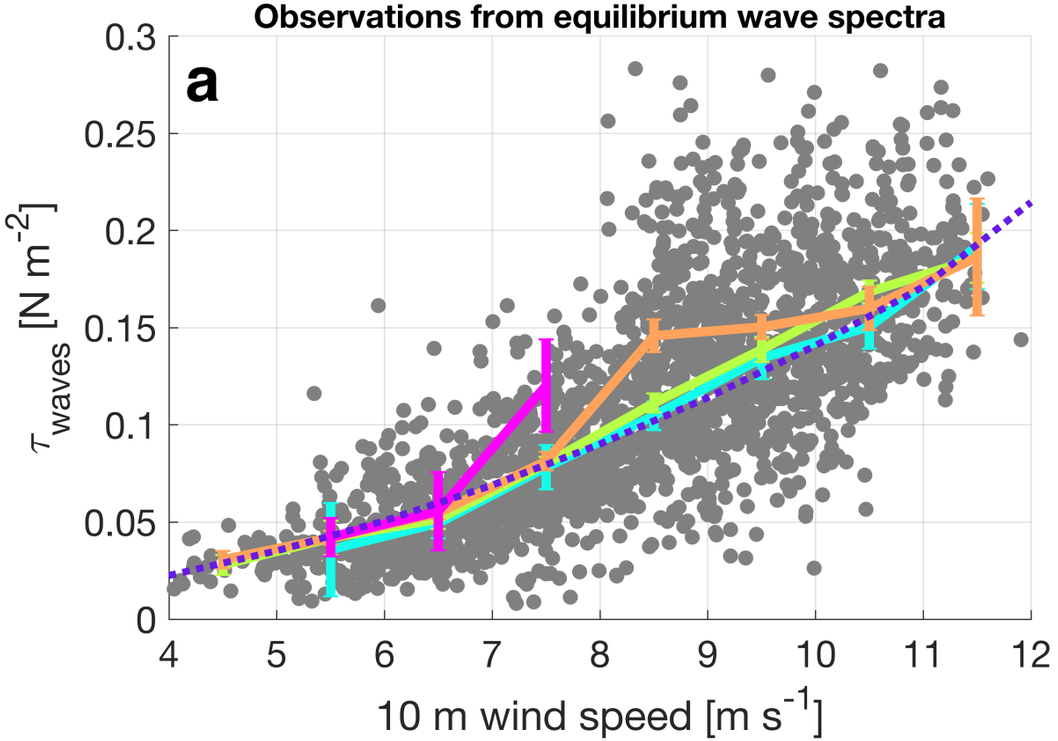
Observations from equilibrium wave spectra
a
τ_{waves} [N m^{-2}]
10 m wind speed [m s^{-1}]

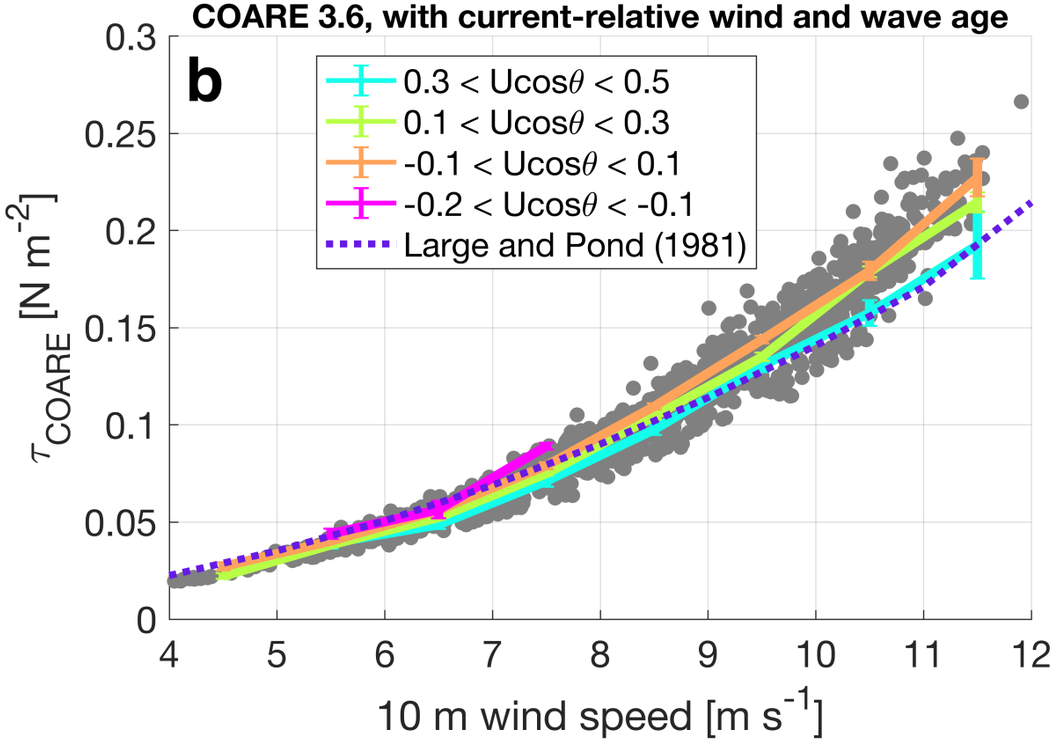
COARE 3.6, with current-relative wind and wave age
b
0.3 < Ucosθ < 0.5
0.1 < Ucosθ < 0.3
-0.1 < Ucosθ < 0.1
-0.2 < Ucosθ < -0.1
Large and Pond (1981)
τ_{COARE} [N m^{-2}]
10 m wind speed [m s^{-1}]

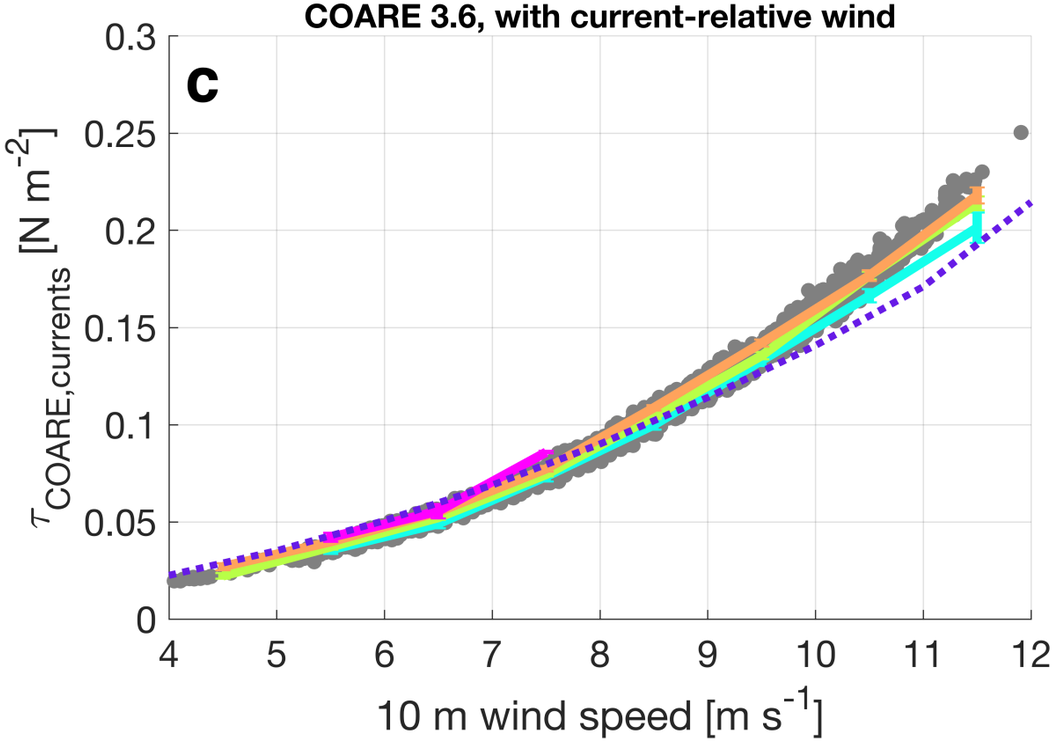
COARE 3.6, with current-relative wind
c
$\tau_{COARE,currents}$ [N m^{-2}]
10 m wind speed [m s^{-1}]

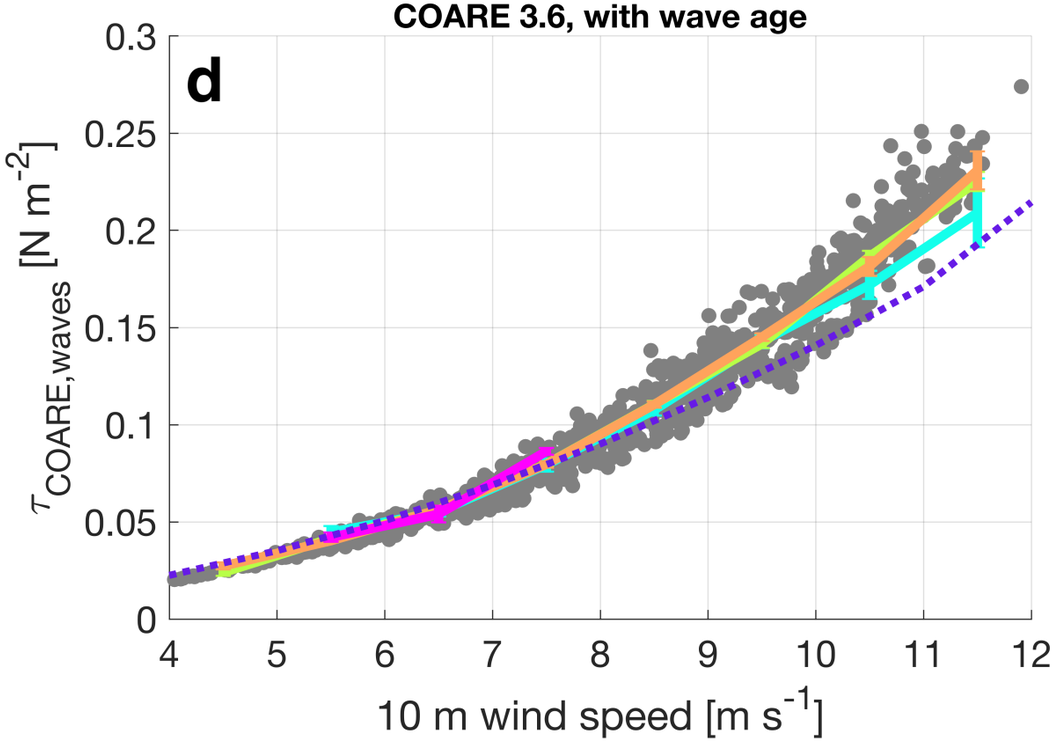
COARE 3.6, with wave age
d
$\tau_{COARE,waves}$ [N m^{-2}]
10 m wind speed [m s^{-1}]

Figure 11.

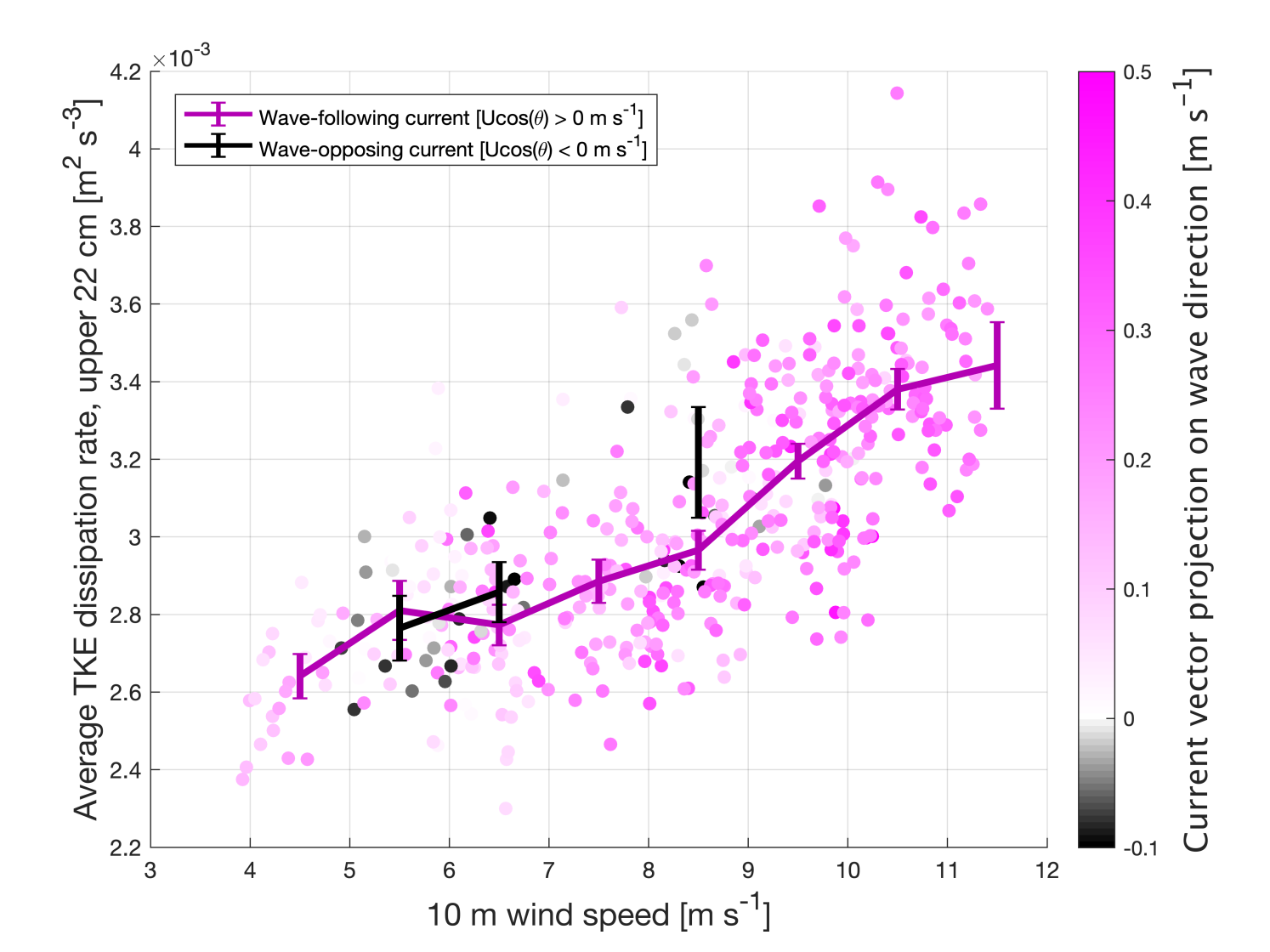
×10^-3
4.2
4
3.8
3.6
3.4
3.2
3
2.8
2.6
2.4
2.2
Average TKE dissipation rate, upper 22 cm [m^2 s^-3]
Wave-following current [Ucos(θ) > 0 m s^-1]
Wave-opposing current [Ucos(θ) < 0 m s^-1]
3
4
5
6
7
8
9
10
11
12
10 m wind speed [m s^-1]
0.5
0.4
0.3
0.2
0.1
0
-0.1
Current vector projection on wave direction [m s^-1]